Title
SOME APPLICATIONS OF TRANSMISSION ELECTRON MICROSCOPY IN MATERIALS SCIENCE AND ENGINEERING

Author
Thomas, Gareth.

Publication Date
1973-04-01

Lecture presented at the International School of Electron Microscopy (Center for Scientific Culture) Erice, Trapani, Sicily, April 7-21, 1973

LBL-1473
c.1

SOME APPLICATIONS OF TRANSMISSION ELECTRON MICROSCOPY IN MATERIALS SCIENCE AND ENGINEERING

Gareth Thomas

April 1973

Prepared for the U. S. Atomic Energy Commission
under Contract W-7405-ENG-48

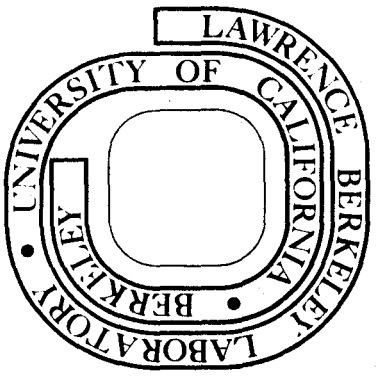

LBL-1473
c.1

DISCLAIMER

SOME APPLICATIONS OF TRANSMISSION ELECTRON MICROSCOPY IN MATERIALS SCIENCE AND ENGINEERING

Gareth Thomas
Professor of Metallurgy
Department of Materials Sciences and Engineering
University of California
Berkeley, California 94720

GENERAL REMARKS

It has long been the aim of metallurgists, and now in a more general way, of material scientists, to be able to learn enough about the relation between microstructure and properties that it becomes possible to design a material from first principles for particular applications. In physical metallurgy, we are just entering such an era, expecially in the design of strong tough alloys.

The role of electron microscopy in this development is essential, if control of microstructure is to be achieved. The situation is less advanced in the case of engineering ceramic materials, partly because they are more complex and because they are difficult to prepare suitably thin for transmission electron microscopy. Similarly, many organic solids of interest cannot be studied easily because of the problem of radiation damage which causes specimen destruction through such processes as bond breaking, ionization, cross-linking, etc. In these latter cases, the high voltage electron microscope is particularly important because a) the greater penetration (Fig. 6, Chapter 1) enables thicker specimens to be examined, thereby minimizing specimen preparation difficulties, b) there is a reduction in radiation damage with increasing energy. However, at certain threshold energies, knock-on damage occurs in which atoms are ejected from their lattice sites. In metals, this effect is one of major importance because 1) such damage can be studied directly in the microscope;

hence it is a powerful technique for understanding problems of major interest in reactor technology (e.g. swelling) especially in view of the energy crises and the need for safe application of nuclear reactors, 2) knock-on damage modifies the microstructure and from this viewpoint determines the maximum operating voltage.

In the present paper, some examples of current research in my group on metallurgical (Part 1) and ceramic materials (Part 2) is given. Other examples have been reviewed recently (1).

PART 1

SOME METALLURGICAL APPLICATIONS - ROLE OF PHASE TRANSFORMATIONS

1. CHALLENGE OF ALLOY DESIGN

Commercial alloys are complex and are put into service after various heat treatments, which invariably involve one or more types of phase transformations. The modern aeroplane is a good example: aluminum alloys used in the superstructure are precipitation hardened, and the microstructures suffer the constraints of heterogeneous nucleation and growth; the landing gear and engine mounts are made from quenched and tempered steels which involves martensitic followed by precipitation reactions; the engines include blades made from superalloys in which ordering transformations occur.

The problem of design for the materials scientist is to produce materials which have all the desirable in-service properties, and microstructure. Although great progress has been made in advanced technology, service failures are still too common, for example mechanical failures in ships and bridges and aeroplane landing gears.

Similarly, control of electrical and magnetic materials requires a better appreciation of the importance of microstructure. This aspect is illustrated in a recent review discussing semiconductor materials by

Meieran and Cass (2). These authors emphasize the necessity for utilizing all of the modern techniques for characterizing structure.

A basic part of alloy design is that of understanding, controlling and utilizing phase transformations (see for example ref. 3). Transformations involving nucleation and growth suffer from heterogeneous nucleation, e.g. at grain boundaries, (Fig. 1a) leading to precipitate free zones PFZ (4), and in other regions in the matrix such as at dislocations. This non-uniformity of structure leads to preferential plastic flow in the regions of lower yield strength e.g. in the PFZ, and generally poor toughness. Attempts to avoid these problems in Al alloys have included thermal mechanical processing (5) and minor alloying additions (6,7). An alternative approach is to utilize homogeneous transformations in which there is no nucleation barrier e.g. spinodals (8-10). Fig. 1(b) shows the uniform nature of the precipitate morphology, expecially at grain boundaries, and in principle such microstructures should lead to good toughness properties. However, even in such cases, intergranular embrittlement is observed and in the following section, the use of several techniques is described in an attempt to understand the reasons for this behaviour.

2. INTERGRANULAR EMBRITTLEMENT IN SPINODAL CU-NI-FE ALLOYS

The microstructural changes occurring during spinodal decomposition of Cu-Ni-Fe alloys have recently been reported, (9,10) and the change in yield strength of the aged alloys has been correlated with the particle size, the composition and the relative volume fraction of the two phases. The yield strength is not determined by the wavelength, but rather by the difference in composition between the two phases. In these studies, it was observed that the aged tensile specimens failed intergranularly with

elongations to fracture of ≈10%, i.e. the grains were ductile, but failure occurred at grain boundaries in spite of the apparent homogeneity of the structure (Fig. 1b). Work has been done to analyze why spinodally decomposed Cu-Ni-Fe alloys failed intergranularly and to determine the grain-size effect for this mode of failure (11).

An alloy containing (in weight percent) 65% Cu-27% Ni-9% Fe was annealed in three batches using different annealing temperatures and times to give three grain sizes ranging from 6μ to 90μ. The grain diameters d, were measured from optical micrographs using the linear intercept method. Standard flat tensile specimens and 2.5 in. square fracture toughness specimens were fabricated from the annealed material. The specimens were then solution treated at 1050°C, water quenched and aged for one hour at 625°C to give the maximum yield strength as reported by Livak and Thomas (10). The fracture toughness specimens were fatigue cracked and then loaded to failure using a MTS testing machine. The metallography was done using light optical and scanning and transmission electron microscopy.

The graph given in Fig. 2 shows the linear dependence of the experimentally measured yield stresses and stress intensities on $d^{-1/2}$. The elongations to fracture were measured on 1 in. gage length tensile specimens, and the values ranged from 29% for the small grain size decreasing to 18% for the large grain size. The k_i values are plane stress rather than plane strain values because of the large plastic zone which preceded fracture. Furthermore, the stress intensity was measured at the onset of crack growth so that this is not the critical stress intensity, but rather the stress intensities for initiation of slow crack growth. The

small grain size specimen failed on two orthogonal shear planes which were 45% to the fatigue crack, whereas the intermediate grain size specimen failed along one shear plane at 45° to the fatigue crack and the large grain size specimen has a relatively flat, but faceted, fracture with shear lips along the edges.

During fracture testing, the crack in the small grain size specimen propagated by a dimpled tearing mechanism with small ledges on the fracture surface that appear to be grain boundaries. For the large grain size specimen, the crack propagated intergranularly with appreciable plastic deformation as evidenced by the dimpled surfaces and the tearing. Some of the relatively flat grain boundaries have the appearance of wavy or serpentine glide which is indicative of ductile fracture mode. The fracture surface of the intermediate grain size specimen showed definite failure along some grain boundaries, although not as pronounced as in the large grain size specimen, with numerous tear ridges and dimples. Fig. 3 shows scanning fractographs which illustrate these features.

Optical metallography of the heat treated specimens showed that along some of the grain boundaries discontinuous precipitation had occurred. In the large grain size material, the jagged, saw-toothed morphology of the precipitate was resolvable; whereas, in the small grain size material a definite thickening of some grain boundaries was observed. Transmission electron microscopy showed a characteristic spinodal microstructure with wavy, irregular particles aligned along <100> planes and with a wavelength of 75Å (see Fig. 1b). Because of the randomness of the grain boundary precipitation and the preferential electropolishing that occurred along grain boundaries, no grain boundary precipitates were observed in the thin foils

of the test specimens. However, in samples aged for very long times or at higher temperatures, preferential coarsening of the spinodal microstructure and discontinuous precipitation have been observed at some grain boundaries (e.g. Fig. 4).

Some x-ray microprobe results suggest that solute segregation may be occurring at the grain boundaries in this spinodally decomposed alloy. Microprobe analysis of the grain boundary precipitates observed after aging the alloy for 1000 hours at 625°C showed ≈ 20% increase in the Ni and Fe concentrations at the precipitates compared to the matrix with a corresponding decrease in the Cu concentration. For a sample aged one hour at 625°C, no change in composition was detected at the grain boundaries. But if the grain boundary zone is less than one micron wide (which is the diameter of the electron beam), then it could not be resolved using the microprobe. This experimental evidence suggests the possibility that solute segregation may occur at the grain boundaries during this transformation.

The experimentally observed dependence of yield strength on grain size is readily explained on the basis of macroscopic yielding due to constrained dislocation motion near grain boundaries and which can be represented by the Petch equation. Based on the analysis of Gerberich et al. (12) for age-hardening aluminum alloys, the stress intensity to nucleate fracture at a grain boundary is given by the equation

$$K_{nucl} = (\phi/d)^{1/2} \varepsilon^* \ell_E$$

where ϕ is a constant, d is the grain diameter, ε^* is the fracture strain at the grain boundary, ℓ is the width of the grain boundary region (e.g.

0.5μ in Fig. 4a) and E is Young's modulus. The present experimental results suggest that an equation of this general form may also be valid for the integranular fracture of spinodally decomposed Cu-Ni-Fe alloys. From the experimental observations, it appears that the discontinuous precipitation reaction cases softening and subsequent crack propagation at the grain boundaries. Alternatively, at low aging temperatures and for short aging times, solute segregation or preferential coarsening of the spinodal microstructure at the grain boundaries may be the principal cause of the observed intergranular failure. Current research is concerned with the mechanism of these grain boundary reactions in an attempt to overcome the problem of intergranular embrittlement.

3. TRANSFORMATIONS AND PROPERTIES OF STEELS

1. Martensitic Structures

a. Metastable Austenites - Strain Induced Martensite

The martensitic transformation from the fcc to the bcc phase in metastable austenitic stainless steels such as Fe/18Ni/8Cr is complicated by the presence of the hcp (ε) phase which is always found to be closely associated with the α. Both the transformation products, ε and α, are believed to transform martensitically in that a shape change was observed in each case, although, as pointed out by Wayman in ref. 2, the shape change has not yet been verified to conform to an invariant plane strain. It is possible for these phases to be obtained either by direct quenching of the austenite to below the M_s temperature or by stress-inducing the transformations below M_d temperature ($M_d > M_s$), although it is not clear whether in 18/8 that α can be produced just by quenching.

The structural characteristics of the ε and α phases in these alloys have been widely investigated using transmission electron microscopy in conjunction with x-ray techniques, since the early work of Venables (13). Recent investigations (14) have established the sequence of transformation to be $\gamma \rightarrow \varepsilon \rightarrow \alpha$ and that ε is a thermodynamically stable phase in 18/8. These duplex alloys are of great interest as having potential high strength and corrosion resistance e.g. the yield strength is linearly proportional to the volume fraction of α martensite (15). The martensite is obtained by plastic deformation at temperatures between M_s and M_d, both of which depend on composition, and vary from alloy to alloy. Invoking the rule of mixtures, it is possible to predict the mechanical properties of such alloys as shown by Gerberich et al. (16). By controlling the transformation, a new class of tough strong steels has been developed (17). However, there is still a lack of knowledge of the factors controlling α morphology, orientation dependence of M_d (if any) and the mechanism of the stress induced martensitic transformation. Thus, we have embarked upon a program using single crystals of an Fe-15Ni-15Cr alloy in order to analyse the transformation $\gamma \rightarrow \varepsilon \rightarrow \alpha$ for crystals oriented for single, duplex and multiple slip, using x-ray and light and electron microscopy techniques (18). The orientation relationships γ-α are of the Kurdjomow-Sachs type (K-S). (See refs. 19,20 for details of the crystallography of martensitic transformations).

An advantage of single crystal work is that the crystallography can be studied in detail and also the morphology of the transformed regions, as can be seen in Fig. 5. The volume fractions of transformed phases are found by x-ray analysis.

New results have been obtained with single crystals in $[\bar{2}\bar{1}3]_\gamma$ pulled to 5% tensile strain at a temperature of 185°K (about 15° below M_d). This is the single glide orientation. The crystals transformed to 6% α martensite and 2% ε martensite by volume. About 80% of the α martensite had the K-S variant of the orientation relationship

$$(\bar{1}11)_\gamma \,||\, (110)_\alpha \; [01\bar{1}]_\gamma \,||\, [\bar{1}1\bar{1}]_\alpha .$$

An interesting point is that the slip system in austenite is also $(\bar{1}11)$-$[01\bar{1}]$. As is seen, the KS variant has both the austenite slip plane and slip direction. Fig. 5 shows the $(\bar{1}11)_\gamma$ and $(01\bar{1})_\gamma$ orientations of this crystal. From the optical micrographs it is observed (by selectively etching the γ-α boundary) that α exists as needles lying in the $(\bar{1}11)_\gamma$ plane. The electron micrographs show the α martensite needles bounded by sheets of ε martensite. The ε plates are the dark bands lying in the $(\bar{1}11)$ slip planes. Epsilon martensite is always present parallel to the slip plane. Neither epsilon nor α martensite form in undeformed regions. We believe the reason α needles are not forming in association with KS variants other than those in the slip plane is because of the confining effect of the first formed ε sheets. The ε plates appear to extend completely over the slip plane.

The dislocation structure is currently being analysed in an attempt to learn more about the nucleation of the α- needles. It has been found that M_d is a function of the critical resolved shear stress of the martensite habit plane as well as temperature. In the 15/15 alloy, the M_d is suppressed as the tensile axis of the crystal moves from $[1\bar{1}0]_\gamma$ to $[100]_\gamma$.

b. Martensites and Tough, Strong Steels

Low alloy structural steels (< about 0.4% carbon and containing small amounts of Ni, Cr, Mo and other elements) can be quenched from the austenite temperature (≈1100°C) so as to transform to martensite below the M_s temperatures. Such steels are then invariably tempered to improve toughness, although there is no fundamental reason for all martensites to be intrinsically brittle. However, there appears to be a correlation between martensite substructure and embrittlement. In untempered steels, if the composition is adjusted such that martensite is internally dislocated rather than twinned (21), one can obtain strong tough martensite even without tempering. The apparent relationship between the transformation substructure, strength and toughness is shown in Fig. 6 for a series of Fe-Ni-Co-C steels (22) which are of interest for applications in aircraft components such as landing gears. This correlation has lead to a systematic investigation of the factors which control the transformation substructure and mechanical properties (see Ref. 21 for review).

The basic crystallographic features of martensite have been discussed by Wayman (19,20). The complex defect substructure of martensite arises because of the inhomogeneous shear component of the transformation strain. It has been proposed (21) that it is the relative critical resolved shear stresses (CRSS) for slip and twinning over the transformation temperature range M_s-M_f that determines whether martensite is dislocated or twinned or both. The twinning can be complex and the analyses described in Chapter 1 must be followed if the structure is to be quantitatively characterized. Fig. 7 shows typical examples of martensitic structures. Since the CRSS for slip in bc crystals increases rapidly at low temperatures, the M_s-M_f temperature range can be regarded as a useful parameter

in designing martensitic alloys to avoid twinning. Since carbon has the most dramatic effect on lowering M_s, we believe 0.4% carbon (in solution) represents the maximum possible carbon content. A simple, ternary Fe-Cr-C as quenched martensitic alloy has been designed to meet these criteria, which has properties equal or superior to existing more complex (and more expensive) steels (23).

Tempering martensite produces precipitation of cementite (Fe_3C) and other carbides. The morphology depends upon the martensitic substructure, the composition and tempering temperature, and Figs. 8,9 show typical examples. In the absence of secondary hardening (hardening due to precipitation of alloy carbides such as molybdenum carbides), the tempering range producing interlath carbides should be avoided because the toughness deteriorates and intergranular embrittlement occurs. This effect is similar to that in aluminum alloys (compare Figs. 1a and 8g).

Characterization of these complex microstructures requires repeated application of dark field imaging as Fig. 7-9 illustrate.

c. Isothermal Transformations - Bainites

If austenite in a low alloy steel is held at a temperature above M_s, it will decompose isothermally into a product of deformed ferrite and carbide called bainite (2) which closely resembles the structure of tempered martensite. Two generally distinct morphologies known as upper (high temperatures) and lower (low temperatures) bainite occur. Typical examples are shown in Fig. 10. The upper bainite is not of much technical interest since the interlath carbides cause embrittlement, again in a similar manner to that shown in Fig. 1a and 8g.

Lower bainite, however, has potential for high strength and toughness at higher carbon levels than seems feasible for martensites. In fact, high carbon Fe/Ni/Co/C alloys show higher toughness and strength when transformed to lower bainite than after quenching to martensitic (22).

The transformation mechanism of austenite to bainite has been a topic of argument for many years. The precipitation process, especially the initial stage, in the bainitic transformation, is not thoroughly understood. The characterization of the nature and the crystallography of carbide phase are important in order to understand the structural features of bainite. It is generally accepted that cementite Fe_3C constitutes the carbide phase in upper bainite. Although cementite is frequently observed in lower bainite, the exact carbide precipitation process is still uncertain. It has been suggested by Oblak and Hehemann (25) that epsilon carbide is the first carbide formed in low temperature bainite. Since the carbide precipitation in steel may assume many different forms such as epsilon carbide, Hägg carbide, cementite, etc., depending on the transformation temperature and time, as well as composition of the steel, the characterization of carbide must be approached with great care. Unfortunately, it is frequently not possible to unambiguously determine the nature of the carbides present because of competing factors and their complex structures.

In order to try to understand these complexities, we are currently investigating (26) the nature of bainite in a wide range of alloys (differing composition and transformation temperature). One steel viz., Fe-0.54C-1.87Si with M_s temperature of 250°C has been isothermally transformed to lower bainite at 275°C. Fig. 11 shows the structure to consist

of a high density of carbide precipitates uniformly distributed throughout the bainitic ferrite matrix. These carbides form as thin platelets laths varying in size from 60 to 200Å wide and 700 to 4000Å long. The corresponding selected area diffraction pattern is shown in the insert together with its indexing. The matrix is in $(100)_\alpha$ zone and the carbide is analyzed as epsilon carbide which orients at about five degrees from the $(11\bar{2}0)_\varepsilon$ zone. In addition to the identification of epsilon-carbide in lower bainite, the orientation relationship between epsilon-carbide and bainitic ferrite may be obtained by stereographic projection analysis, and from Fig. 11 we obtain

$$(0001)_\varepsilon \text{ " } (011)_\alpha$$

$$(10\bar{1}1)_\varepsilon \text{ " } (101)_\alpha$$

which is the same as the orientation relationship suggested by Jack (27) for tempered martensites.

This new observation of the existence of epsilon-carbide in lower bainite further confirms the transformation mechanism that lower bainite forms initially as supersaturated ferrite from which epsilon-carbide precipitates very rapidly and is subsequently replaced by cementite upon further transformation. Also, it is evident that the nature of the carbide phase that exists in lower bainitic structures depends on the transformation temperature and time as well as on the composition of the steel under investigation.

References Chapter

Part I

1. W. L. Bell and G. Thomas, Electron Microscopy and Structure of Materials, (Ed. G. Thomas), Univ. Calif. Press, 23 (1972).

2. Phase Transformations , Amer. Soc. Metals (1970).

3. E. S. Meieran and T. R. Cass, Electron Microscopy and Structure of Materials, (Ed. G. Thomas), Univ. Calif. Press, 1027 (1972).

4. G. Thomas and J. Nutting, J. Inst. Metals, 88, 81 (1959-60).

5. G. Thomas, ibid, 89, 287 (1960-61)

6. B. Noble, Acta Met. 16, 393 (1968).

7. S. K. Das, G. Thomas and D. Rowcliffe, Microscopie Electronique, 2, 533 (1970).

8. J. W. Cahn, Trans AIME, 242, 166 (1968).

9. E. P. Butler and G. Thomas, Acta Met., 18, 347 (1970).

10. R. J. Livak and G. Thomas, ibid., 19, 497 (1971).

11. R. J. Livak and W. W. Gerberich, Electron Microscopy and Structure of Materials,(Ed., G. Thomas,) Univ. Calif. Press, 647 (1972).

12. W. W. Gerberich, V. F. Zackay, E. R. Parker and D. Porter, Ultra Fine Grained Metals (Syracuse Univ. Press), 259 (1970).

13. J. A. Venables, Phil. Mag., 7, 35 (1962).

14. P. R. Manganon and G. Thomas, Met. Trans., 1, 1586 (1970).

15. P. R. Manganon and G. Thomas, Ibid., 1, 1577 (1970).

16. W. W. Gerberich, G. Thomas, E. R. Parker and V. F. Zackay, "Strength of Metals and Alloys," (2nd Int. Conf. Asilomar, Calif.) Amer. Soc. Metals, 3, 894 (1970).

17. V. F. Zackay, E. R. Parker, D. Fahr and R. Busch, Trans. Amer. Soc. Met., 60, 252 (1967).

18. G. A. Stone, Ph.D. Thesis (in progress), M.S. Thesis, LBL report 134 (1971).

19. C. M. Wayman, Introduction to the Crystallography of Martensitic Transformations , McMillan Co., (1964).

20. C. M. Wayman, Modern Diffraction and Imaging Techniques in Materials Science, (Ed. S. Amelinckx et al.) N. Holland Press, 187 (1970).

21. G. Thomas, Met. Trans., 2, 2373 (1971).

22. S. K. Das and G. Thomas, Trans. Amer. Soc. Met., 62, 671 (1969).

23. J. A. McMahon and G. Thomas, Proc. International Conf. on Strength of Materials, Cabmridge, United Kingdom 1973, Inst. of Metals (London) in Press.

24. R. F. Hehemann, Phase Transformations , Amer. Soc. Metals, 397 (1970).

25. J. M. Oblak and R. F. Hehemann, Transformation and Hardenability in Steels, Climax Molybdenum Co., 15 (1967).

26. D. Huang, Ph.D. Thesis (in progress)

27. K. H. Jack, J. Iron and Steel Inst., (London), 169, 26 (1951).

CHAPTER FIGURE CAPTIONS

Part I

Fig. 1. Microstructures from aging reactions in alloys (a) Non-uniform microstructures due to preferential nucleation at grain boundaries in Al-Mg-Zn. The variation in nucleating conditions can be inferred from the variation in size and density of particles which occurs with distance from the boundaries. Bright field (Ref. 4 Courtesy Inst. Metals). (b) Apparent uniform microstructure in spinodally transformed Cu-Ni-Fe alloy. The lower grain is in a strong diffracting orientation and is thus in dark contrast. (Bright Field). The contrast modulations indicate periodic fluctuations in composition along <001>. The wavelength increases with aging time and temperature (compare to Fig. 21, Chapter I).

Fig. 2. Stress intensity and yield stress values plotted as a function (grain diameter)$^{-1/2}$ showing the linear dependence of these two parameters on $d^{-1/2}$. (Ref. 11 courtesy Univ. Calif Press).

Fig. 3(a) Scanning electron fractograph of the small grain size fracture specimen showing the ductile nature of the fracture as evidenced by dimples in the grains. (b) Low magnification scanning electron fractograph of the large grain size fracture specimen showing the intergranular fracture; notice dimples within grains.

Fig. 4(a). Dark field electron micrograph of this Cu-Ni-Fe alloy aged for 10 hours at 700°C showing discontinuous precipitation at the grain boundary. (b) Bright field electron micrograph of this alloy aged for 10 hours at 775°C showing enhanced particle coarsening along the grain boundary. (Ref. 11, Courtesy Univ. Calif. Press)

Fig. 5. Fe-15Ni-15Cr Single crystal in $[\bar{2}\bar{1}3]$ after 5% tensile deformation showing two (perpendicular) surface analysis by light and electron

optical techniques: A,B thin foils bright field showing that the α-phase forms as needles between the sheets of ε, C,D are corresponding light micrographs. a = α-martensite, b = epsilon on $(\bar{1}11)$ c = austenite (Courtesy G. A. Stone).

Fig. 6. Showing the relationship between yield strength and fracture toughness for a series of Fe/Ni/Co/C steels. Notice at the same yield stress the dislocated martensite is tougher than the twinned martensite as shown by the bright field images (twins marked T) (Ref. 22 courtesy Amer. Soc. Met.).

Fig. 7(a). is a bright field image of as-quenched martensite in Fe-25Ni-10Co steel. The dislocated lath structure is typical of low carbon martensites and yields high toughness with moderate to high tensile strength. (b) shows the bright field image of a twinned martensite plate in Fe-28.5 Ni-10 Co steel. (c) is a related dark field image of twin reflection. The corresponding selected area diffraction pattern is shown in (d), and indicates the dark field image is formed by superimposed twin and matrix reflections. The complexity of the substructure, with matrix dislocations and multiple twinning, is revealed by this technique. Twinned martensite normally occurs when carbon content exceeds approximately 0.3% or in general when th total solute content increases. Except for cobalt, increasing the solute content also lowers the M_s temperature. The presence of a high twin density in a martensitic structural steel has been found to be associated with low fracture toughness and high yield strength. (Courtesy S. K. Das).

Fig. 8. Dark field imaging is an essential technique for determining the distribution and orientation of carbide precipitates in tempered martensites. (e) is the dark field image of a carbide reflection in Fe-9 Ni-4 Co-0.45 C steel tempered at 500°F for 4 hours, showing the precipitation of epsilon carbide on {100} martensite planes. The initial formation of Fe_3C on {110} martensite planes is seen at A. Epsilon carbide will precipitate only at low tempering temperatures and dissolves upon formation of Fe_3C at higher temperatures. (f) illustrates the dark field image of a Widmanstatten pattern of Fe_3C in Fe-4Cr-5.3Co-0.35C tempered at 400°F for 4 hours. This precipitate substructure is found in almost all dislocated martensites tempered at low temperatures, as well as in as-quenched martensites which undergo autotempering due to their high M_s temperatures. The formation of a Widmanstatten pattern of Fe_3C is accompanied by "normal" tempering behavior, viz., an increase in fracture toughness and a decrease in yield strength. At higher tempering temperatures, carbides may precipitate along martensite lath boundaries, causing a marked decrease in toughness. (g) shows a dark field image of interlath carbides in the same alloy as in (f) tempered at 800°F for 4 hours. At very high tempering temperatures, the carbides spherodize producing an increase in toughness and a further reduction in yield strength. A dark field image of spherodized carbides is shown in (h), which is the same steel as in (f) tempered at 1000° F for 4 hours. (Courtesy S. K. Das and M. R. Raghavan).

Fig. 9. When twinned martensites are tempered, the carbides precipitate along the twin boundaries. The twin boundary carbides have been

associated with a decrease in fracture toughness in structural steels. (i) is a bright field image of a twinned martensite plate in Fe-27 Ni-10 Co-0.1C steel, where the twin density is highest at the midrib. The steel was tempered at 200°C for 1 hour, and a Widmanstatten pattern of Fe_3C is seen outside the twinned area. (j) shows a dark field image of the twins, and (k) is a dark field image of the unidirectional carbides on the twin boundaries. Note that the particular Fe_3C reflection used in (k) illuminates only the twin boundary carbides and not the Widmanstatten pattern outside the twinned area. This points out the need for imaging several different carbide reflections in order to determine completely the precipitate morphology. These examples illustrate that the tempering behaviour depends on the initial martensitic substructure which can vary within each plate as well as from plate (or lath) to plate. (Courtesy S. K. Das).

Fig. 10(l) is the bright field image of upper bainite in Fe-4Cr-0.34 C steel, and (m) is the dark field image of a carbide reflection, showing the characteristic elongated carbides between the bainitic ferrite laths. Upper bainite, which is formed at high isothermal transformation temperatures, normally has a low fracture toughness. Note the similarity of the carbide morphology in (m) with that shown in (g), a tempered martensite which is likewise embrittled by inter-lath carbides. At lower transformation temperatures, the Fe_3C precipitates unidirectionally within the bainite laths. This is seen in (n), the bright field image of lower bainite in Fe-4Cr-5.3Co-0.35C steel. The dark field image in (o) reverses the contrast of the carbides. Normally the carbides in lower bainite form at an angle

of 55% to 65% to the long direction of the bainite laths. The carbide morphology of lower bainite in (l) and (m) is similar to that of dislocated martensite tempered at low temperatures, as seen in (e) and (f). Both structures also exhibit high toughness values. It is thus seen that by comparing upper bainite with tempered martensite having interlath carbides, and lower bainite with tempered martensite having Widmanstatten carbides, there is a strong correlation between microstructure and mechanical properties. In steels having a twinned martensitic substructure and poor toughness, it may be preferable to utilize isothermal transformations to produce dislocated lower bainite having a higher toughness due to the similarity of its structure with that of tempered dislocated martensite. (Courtesy S. K. Das).

Fig. 11. Structure of lower bainite which is obtained by isothermal transformation of 0.54C-1.87Si steel at 275°C. Characteristic wavy exsilon carbide particles from 60 to 200Å in wideth and 700 to 4000Å in length are seen in the bainitic ferrite grain. The inset shows the selected area diffraction pattern where the foil orientation is $(100)\alpha$ and the epsilon carbide is about 5 degrees from $(11\bar{2}0)\varepsilon$ orientation. (Courtesy D. Huang).

a b

XBB 695-3420-A

Fig. 1

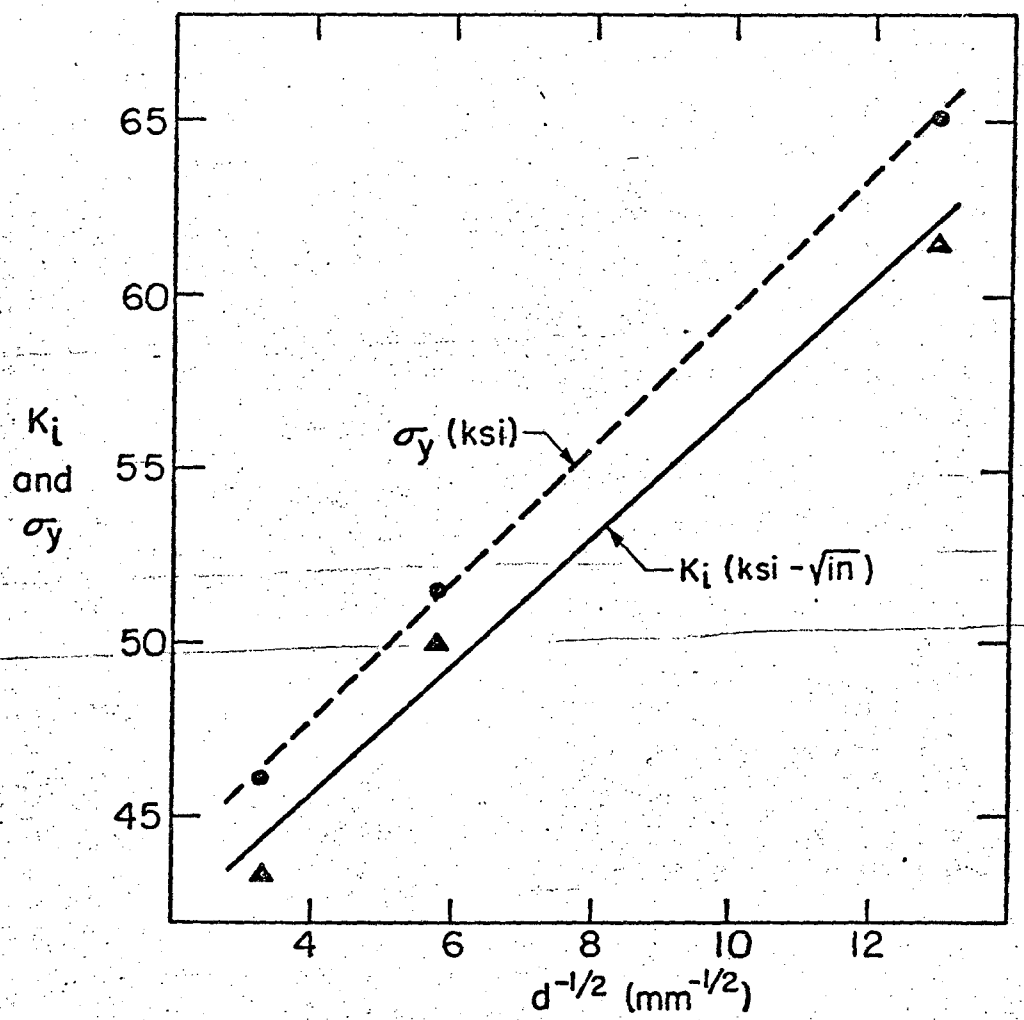
65
60
55
50
45
K_i and σ_y
σ_y (ksi)
K_i (ksi - $\sqrt{in}$)
4
6
8
10
12
$d^{-1/2}$ ($mm^{-1/2}$)
XBL 717-7014

Fig. 2

G. Thomas

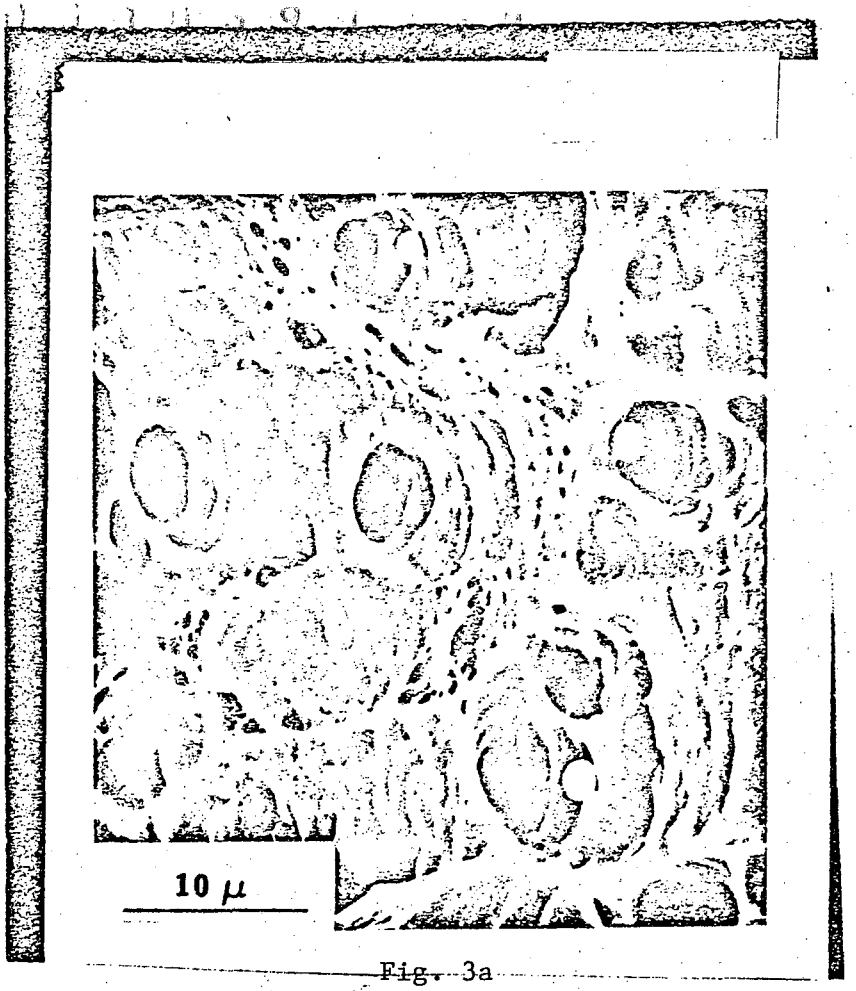

XBB 705 2304

Fig. 3a

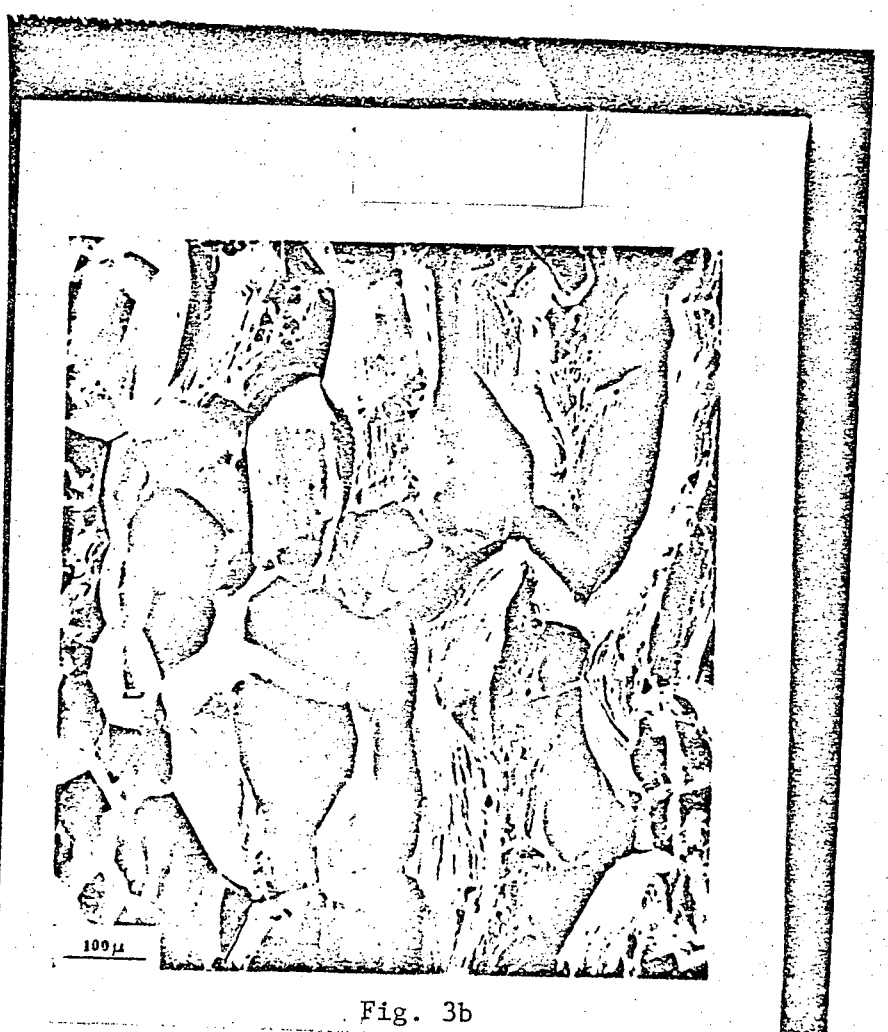

XBB 705 2305

Fig. 3b

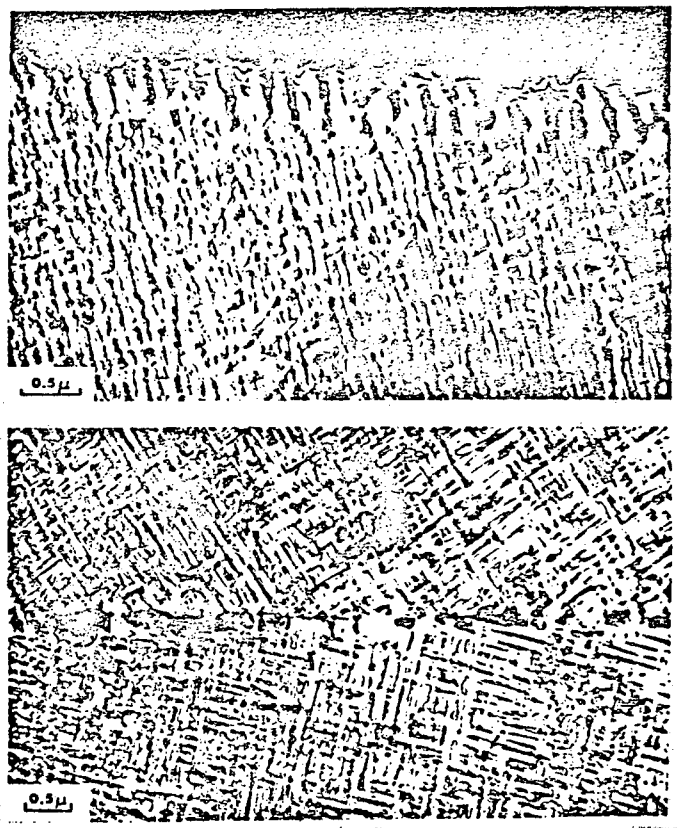

a

b

XBB 719 4167

Fig. 4

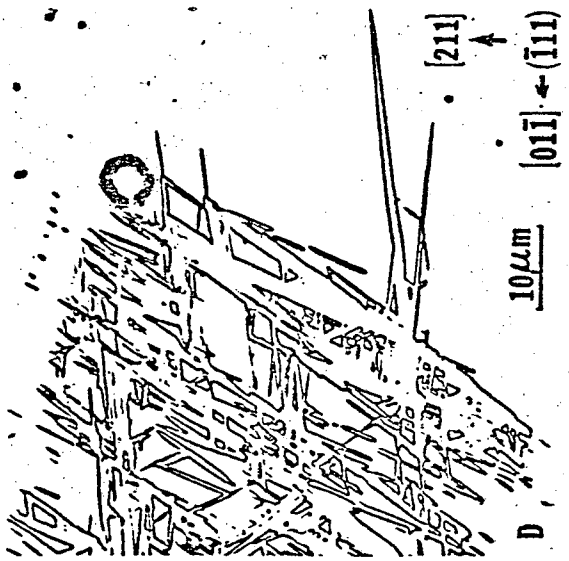

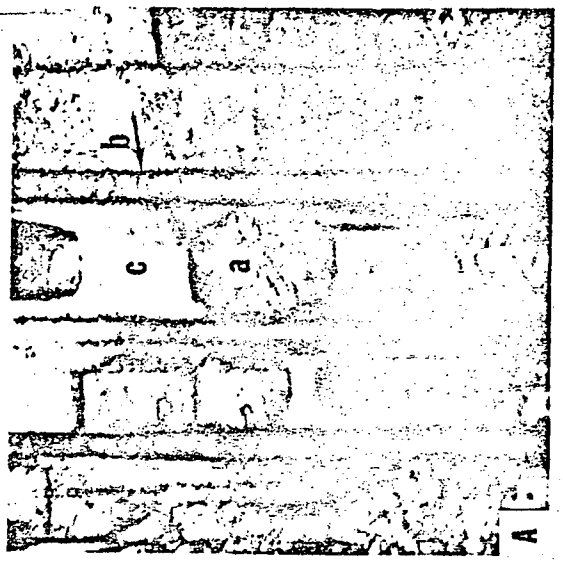

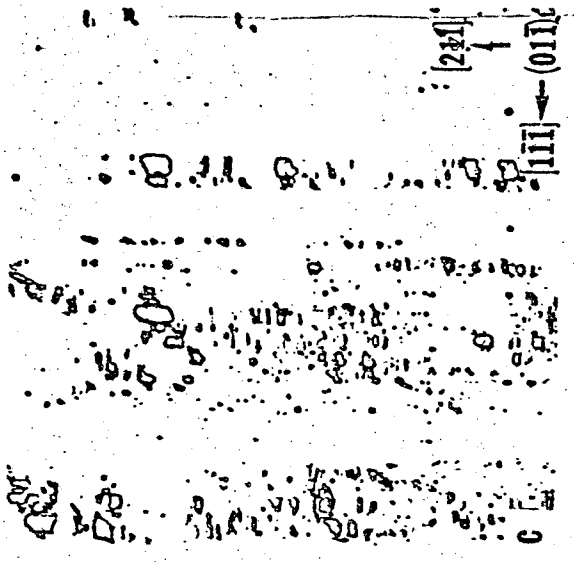

XBB 732-586

Fig. 5

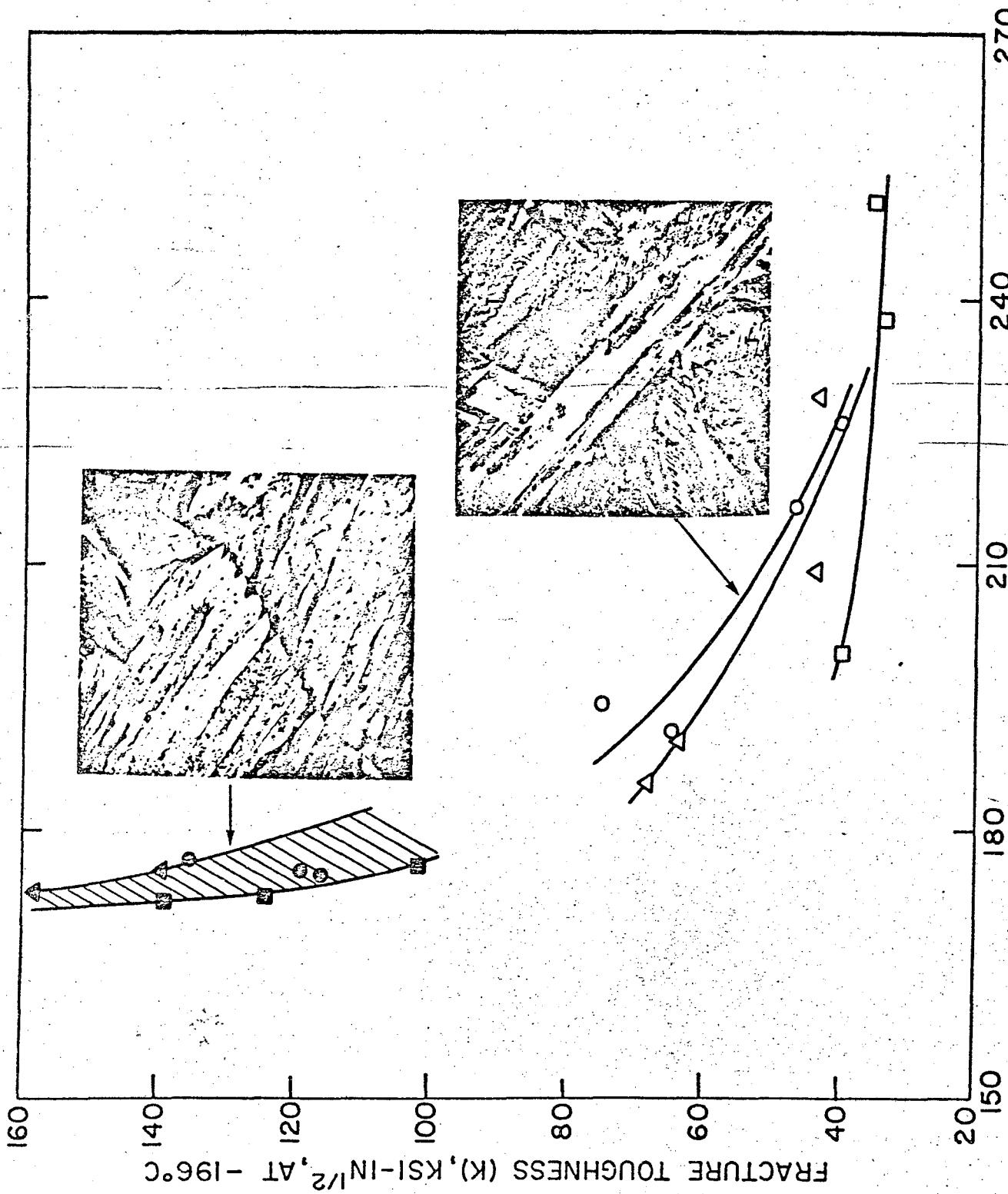

XBB 701-475

Fig. 6

DISLOCATED AND TWINNED AS-QUENCHED MARTENSITES

Magnification: 45,000X

A

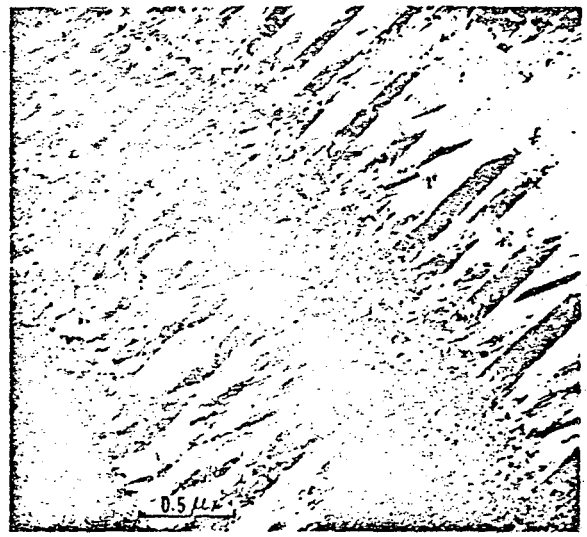

B

Magnification: 56,000X

(A) is a bright field image of as-quenched martensite in Fe-25 Ni-10 Co steel. The dislocated lath structure is typical of low carbon martensites and yields high toughness with moderate to high tensile strength. (B) shows the bright field image of a twinned martensite plate in Fe-28.5 Ni-10 Co steel. (C) is a related dark field image of a twin reflection. The corresponding selected area diffraction pattern is shown in (D), and indicates the dark field image is formed by superimposed twin and matrix reflections. The complexity of the substructure, with matrix dislocations and multiple twinning, is revealed by this technique. Twinned martensite normally occurs when carbon content exceeds approximately 0.3% or in general when the total solute content increases. Except for cobalt, increasing the solute content also lowers the Ms temperature. The presence of a high twin density in a martensitic structural steel has been found to be associated with low fracture toughness and high yield strength.

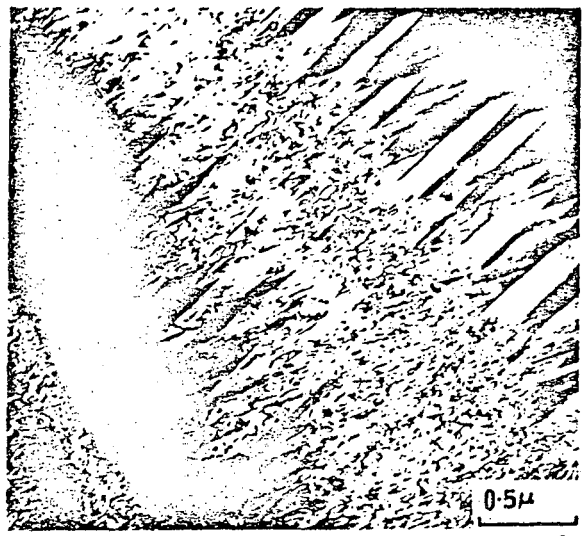

Magnification: 56,000X

C

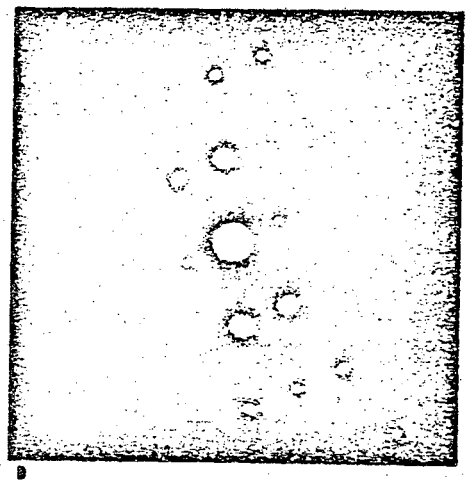

D

Fig. 7

XBB 729-4502

TEMPERED DISLOCATED MARTENSITE

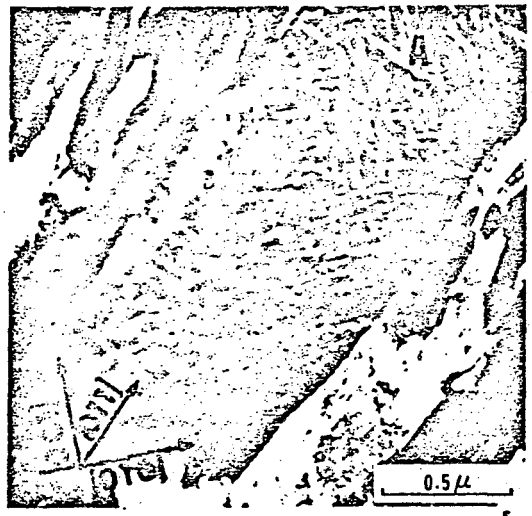

E

Magnification: 76,000X

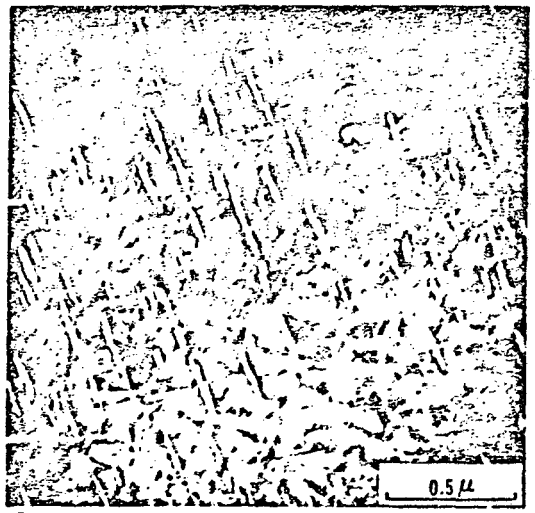

F

Magnification: 75,000X

Dark field imaging is an essential technique for determining the distribution and orientation of carbide precipitates in tempered martensites. (E) is the dark field image of a carbide reflection in Fe-9 Ni-4 Co-0.45 C steel tempered at 400 °F for 4 hours, showing the precipitation of epsilon carbide on {100} martensite planes. The initial formation of Fe_3C on {110} martensite planes is seen at A. Epsilon carbide will precipitate only at low tempering temperatures and dissolves upon formation of Fe_3C at higher temperatures. (F) illustrates the dark field image of a Widmanstatten pattern of Fe_3C in Fe-4Cr-5.3 Co-0.35C tempered at 400 °F for 4 hours. This precipitate substructure is found in almost all dislocated martensites tempered at low temperatures, as well as in as-quenched martensites which undergo autotempering due to their high Ms temperatures. The formation of a Widmanstatten pattern of Fe_3C is accompanied by "normal" tempering behavior, viz, an increase in fracture toughness and a decrease in yield strength.

At higher tempering temperatures, carbides may precipitate along martensite lath boundaries, causing a marked decrease in toughness. (G) shows a dark field image of interlath carbides in the same alloy as in (F) tempered at 800° F for 4 hours. At very high tempering temperatures, the carbides spherodize producing an increase in toughness and a further reduction in yield strength. A dark field image of spherodized carbides is shown in (H), which is the same steel as in (F) tempered at 1000° F for 4 hours.

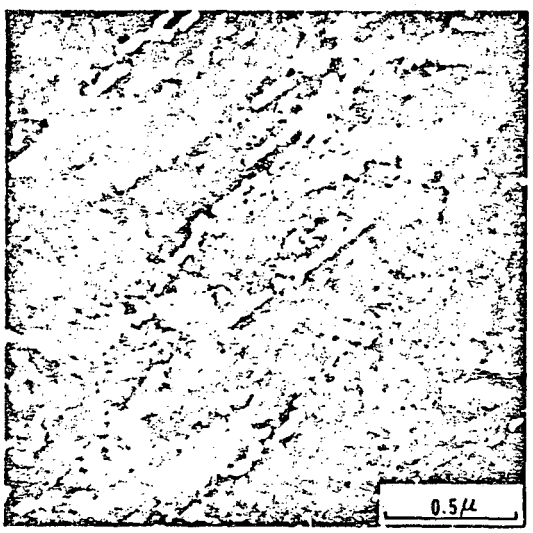

G

Magnification: 77,000X

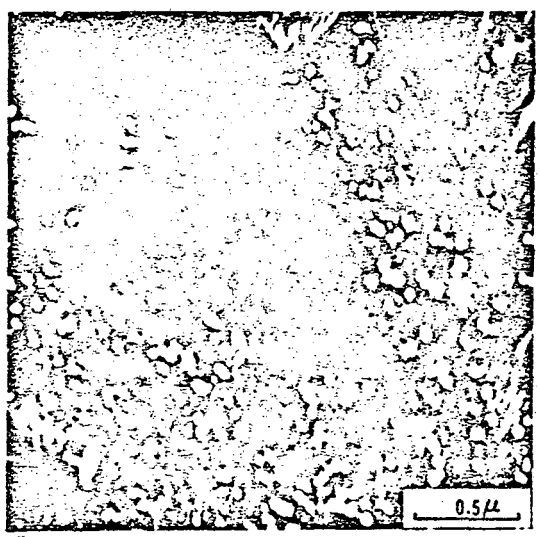

H

Magnification: 60,000X

YBB 729 4504

Fig. 8

TEMPERED TWINNED MARTENSITE

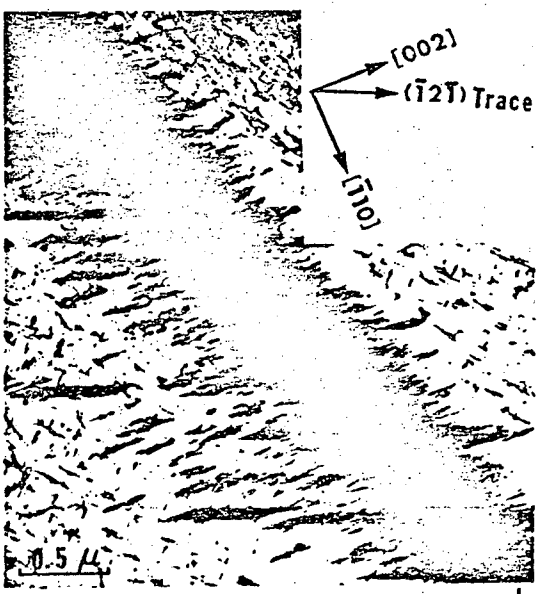

Magnification: 52,000X

I

J

Magnification: 52,000X

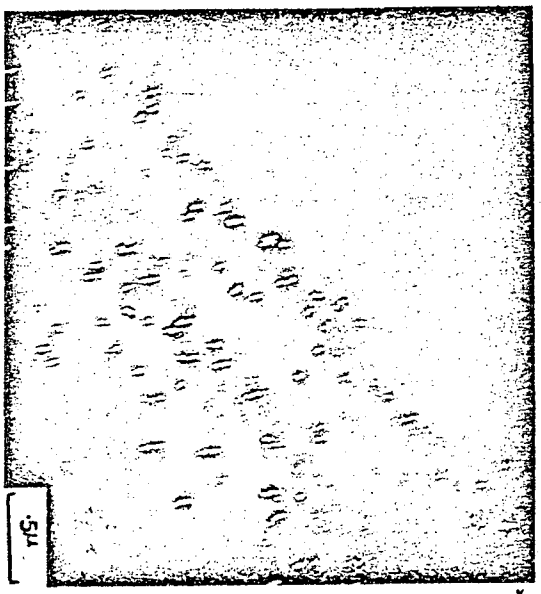

Magnification: 52,000X

K

When twinned martensites are tempered, the carbides precipitate along the twin boundaries. The twin boundary carbides have been associated with a decrease in fracture toughness in structural steels. (I) is the bright field image of a twinned martensite plate in Fe-27 Ni-10 Co-0.1C steel, where the twin density is highest at the midrib. The steel was tempered at 200° C for 1 hour, and a Widmanstatten pattern of Fe_3C is seen outside the twinned area. (J) shows a dark field image of the twins, and (K) is a dark field image of the unidirectional carbides on the twin boundaries. Note that the particular Fe_3C reflection used in (K) illuminates only the twin boundary carbides and not the Widmanstatten pattern outside the twinned area. This points out the need for imaging of several different carbide reflections in order to determine completely the precipitate morphology. These examples illustrate that the tempering behavior depends on the initial martensitic substructure which can vary within each plate as well as from plate (or lath) to plate.

XBB 729-4505

Fig. 9

ISOTHERMAL TRANSFORMATIONS

Magnification: 80,000X

L

M

Magnification: 80,000X

(L) is the bright field image of upper bainite in Fe-4Cr-0.34 C steel, and (M) is the dark field image of a carbide reflection, showing the characteristic elongated carbides between the bainitic ferrite laths. Upper bainite, which is formed at high isothermal transformation temperatures, normally has a low fracture toughness. Note the similarity of the carbide morphology in (M) with that shown in (G), a tempered martensite which is likewise embrittled by interlath carbides.

At lower transformation temperatures, the Fe_3C precipitates unidirectionally within the bainite laths. This is seen in (N), the bright field image of lower bainite in Fe-4Cr-5.3Co-0.35C steel. The dark field image in (O) reverses the contrast of the carbides. Normally the carbides in lower bainite form at an angle of 55° to 65° to the long direction of the bainite laths. The carbide morphology of lower bainite in (L) and (M) is similar to that of dislocated martensite tempered at low temperatures, as seen in (E) and (F). Both structures also exhibit high toughness values. It is thus seen that by comparing upper bainite with tempered martensite having interlath carbides, and lower bainite with tempered martensite having Widmanstatten carbides, there is a strong correlation between microstructure and mechanical properties.

In steels having a twinned martensitic substructure and poor toughness, it may be preferable to utilize isothermal transformations to produce dislocated lower bainite having a higher toughness due to the similarity of its structure with that of tempered dislocated martensite.

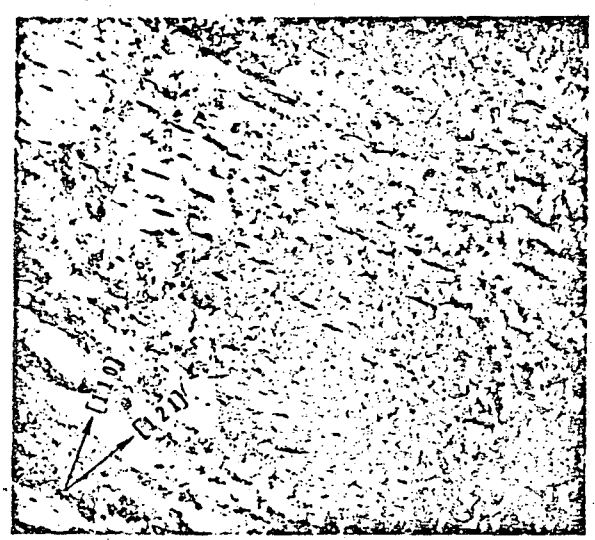

Magnification: 80,000X

N

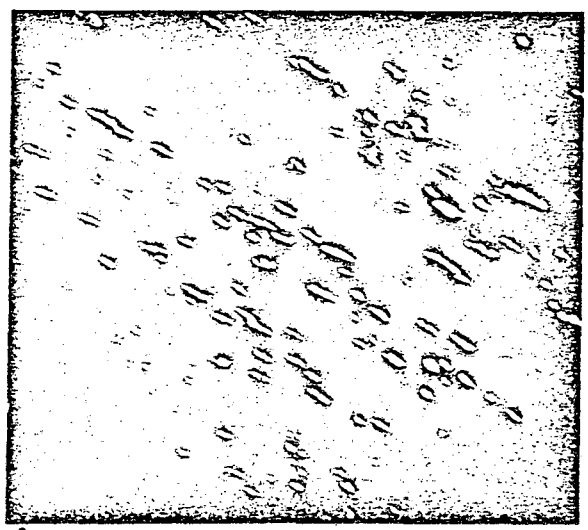

O

Magnification: 80,000X

YBB 729 4503

Fig. 10

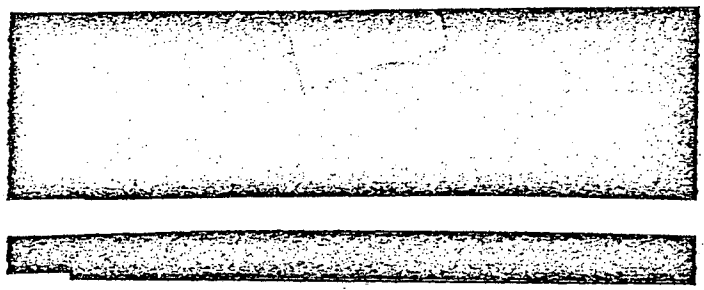

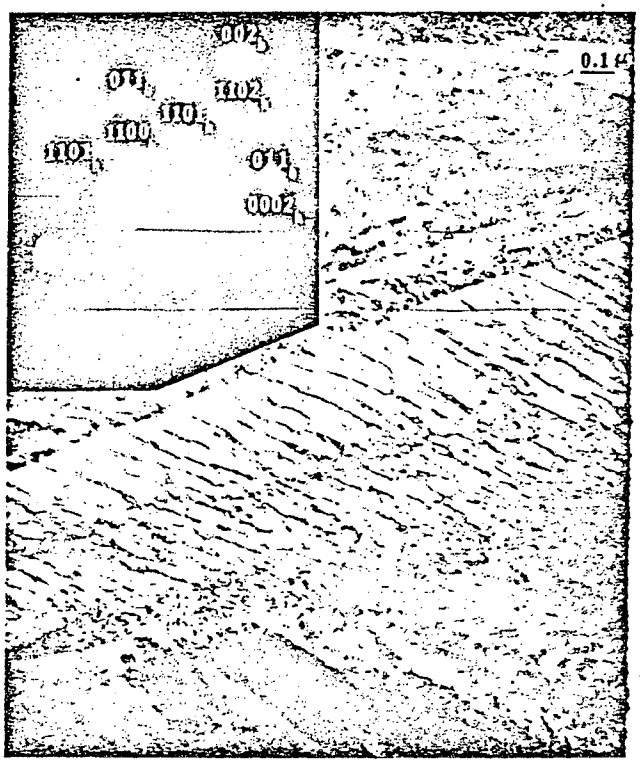

XBB 7212 6112

Fig. 11

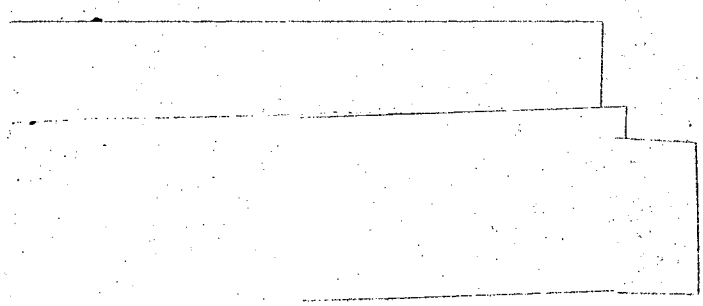

PART 2

CERAMICS AND MINERALS

APPLICATIONS OF HIGH VOLTAGE ELECTRON MICROSCOPY

1. INTRODUCTION

The examination of non-metallic materials is proceeding rapidly at this time, especially at high voltages. This is due to the greater penetration and reduced ionization damage at high voltages, coupled with considerable improvements in specimen preparation techniques such as ion thinning or sputter-etching. It is interesting that the latter techniques were first tried twenty years ago when transmission electron microscopy of crystals was just emerging; but due to the success of chemical and electrochemical thinning techniques especially for metals, ion thinning was not utilized until fairly recently when non-conducting solids started to be examined in detail.

2. ION THINNING

The principles of the latest developments in ion-thinning have been described by Barber (1). A schematic diagram of the apparatus is shown in Fig. 1, which is a modification of a commercial sputtering device.

When preparing thin foils, it is important to keep their temperature sufficiently low to avoid structural changes. Consequently, ion current densities in excess of ≈200 $\mu A/cm^2$ are unnecessary. This is a factor of 10^{-1} to 10^{-2} lower than the ion density in normal sputtering systems. Moreover, if the ion energy is increased beyond ≈ 10 keV, most of the increase is dissipated in deeper penetration (which is clearly undesirable) and not in greater efficiency of sputtering. With care, damage to the surfaces by ion bombardment can be kept to a minimum. However, ion damage in the electron microscope can occur as is discussed later. The ion guns are of the hollow anode type and each produces

one beam. Each anode is connected through a large ballast resistor to a well-stabilized 10 kV, 10 mA DC supply. The bombardment chamber is mounted over a 6 in. diffusion pump and liquid nitrogen trap, backed by a two-stage rotary pump. The vacuum system maintains a working vacuum of between 10^{-3} and 10^{-4} torr while high purity argon gas is entering the anode-cathode interspace through fine needle valves. The main disadvantage of the cold cathode ion source is that it necessitates a relatively large flow of gas into the system. With a typical gas flow rate of $\approx 5 \times 10^{-2}$ torr 1 sec^{-1} there is an ion current of about 70 μA per gun at 6 kV. The ion current density at the sample is about 200 μA cm^{-2}. The ion currents can be measured and balanced by means of retractable probes.

The sample, with its periphery sandwiched in a thin stainless steel holder, is rotated in the ion beams. The inclination of its exposed surfaces with respect to the beams can be preset at angles between 0 and 30°. It is important that the ion beams should "see" both surfaces and erode them at equal rates if no provision is made to stop the back-diffusion of sputtered atoms from the sample and its holder. To minimize the redeposition of sputtered material on the sample, one can place a partial shield around it which is cooled by liquid nitrogen. The shield also prevents the occurrence of arc discharges in the ion guns when thinning materials which give off volatile constituents. Eventually, the ion sources become electrically unstable to glow discharge because of enlargement of the holes in the cathodes. In normal use, however, they have a life of about 250 h.

3. ION DAMAGE

DeJonghe and Thomas (2) observed that ion damage in the form of vacancy defects occurred when cobalt ferrites were examined in the 650 kV microscope. Mass spectometer measurements of the impurities in the objective chamber indicate that nitrogen and oxygen ions are the most likely ones to cause damage (Fig. 2). The density of defects does not seem to exceed about 2×10^9 per cm^2; and, therefore, do not mask other features. Nevertheless, their presence must be recognized as arising "artificially" i.e. they are not characteristic of the normal microstructures. They can be seen as small strain contrast defects in Figs. 8,9.

4. EXAMPLES OF RESEARCH ON SPINELS

a) Introduction

Presently, about thirty different cations are known to form spinels with oxygen. We are studying cobalt and lithium ferrites which are ferrimagnetic, and are thus of interest in the electronics industries e.g., (3). Conventionally, grain size or porosity has been used to control the magnetic properties of polycrystalline ferrites, but it is likely that heat treatments, producing the proper microstructure, could lead to magnetic materials with highly desirable properties. Compared to mechanical properties the field of microsctructural relationship with magnetic properties has hardly been explored. Our results of phase transformation studies in cobalt ferrites over the composition range Co/Fe = 0.54/0.76 have been published previously (4).

The structure of spinels is best understood if attention is focused on the oxygen sublattice. The oxygen sublattice is face centered cubic.

The octahedral and tetrahedral interstices are partially filled with the cations cobalt (or lithium) and iron. These ferrites are inverse spinels, which means that the trivalent ions prefer the tetrahedral sites rather than the regular octahedral sites. Lithium ferrites in the composition range being studied, viz., $LiFe_5O_8$, order below 750°C.

b) Dislocations in Spinels

Except for simple structures, dislocations in oxide crystals have been somewhat neglected by the ceramist, mainly because most highly ionic crystals are very brittle, even up to high temperatures. The efforts in studies of mechanical properties of ceramics have therefore been concentrated on crack formation and propagation on a macroscopic scale. Dislocations play a fundamental role in the mechanical behavior of oxide materials, as they do in metals, and the details of the dislocation structure itself should be of great importance with regard to high temperature deformation, fracture, or creep. Detailed contrast experiments have therefore been carried out to determine the degree of dissociation of dislocations in cobalt ferrite spinels.

The geometry of dislocation dissociation in the spinel lattice has been discussed in detail by Hornstra, (5) who advanced agruments for a four-fold dissociation of a perfect dislocation in spinels. The main agruments are that local electroneutrality can only be maintained in the four-fold dissociated configuration and that in nature spinels are found that are twinned on {111} planes. This observation of twinning in natural spinels was seen as evidence for the presence of Shockley partials. The dislocation reactions are shown in Fig. 3. For two-fold dissociation, the bounding partials have identical Burgers vectors both equal to a/4<110>.

They are bounding a stacking fault in the cation sublattice only, since the fcc oxygen sublattice has actually half the lattice parameter of the spinel lattice. Two-fold dissociation on {100} planes was observed in magnesium aluminate spinels, and the nature of the cation stacking fault has been discussed by Lewis (6). For the four-fold dissociation the two outer pairs of Schockley partials bound a compound fault: an intrinsic stacking fault in the oxygen sublattice plus a fault in the cation sublattice. In this fault, the cations would have moved to their favored crystal coordination.

c. Cobalt Ferrite

The cobalt iron spinels examined were grown by a flux method, and contained only few dislocations. The composition of the crystals varied between $Co_{1.05}Fe_{1.05}O_4$ and $Co_{1.29}Fe_{1.71}O_4$. (7) After examining many specimens, no diffracting conditions could be found where fault contrast between dislocation pairs was in evidence. This in itself is already a strong indication that the isolated dislocations do not have a Burgers vector of $a/4\langle 110\rangle$, but a more positive conclusion could be drawn if the magnitude of the Burgers vector could be determined more directly. (Chapter 2). In strictly two beam diffracting conditions, as can be more closely approximated in 100 kV electron microscopes, the distinction between $\vec{g}\cdot\vec{b} = 1$ and $\vec{g}\cdot\vec{b} = 2$ is relatively clear when the deviation parameter $w_g = 0$. For $\vec{g}\cdot\vec{b} = 1$ the dislocation consists of a single line image, while for $\vec{g}\cdot\vec{b} = 2$ the image shows double lines. At 650 kV the Ewald sphere has appreciably less curvature than at 100 kV, and it is usually not possible to produce two beam diffracting conditions. Instead, the specimen should be tilted to give a set of systematic reflections. Analysis requires

the application of many beam dynamical theory, as indicated in Chapter 2. Reference to Chapter 2 and Fig. 19 provides the basis for the application to dislocations in spinels. The analysis is based on comparing observed and calculated fringe spacings in the image (position of subsidiary maxima or minima) as shown in Figs. 4 and 5. For orientation and $\vec{g}\cdot\vec{b}$ analysis, the silicon Kikuchi maps (8) can be utilized, remembering the small differences in structure factor rules between spinel and diamond cubic lattices.

In Figs. 4 and 5, microphotometer tracings of the dislocation images are compared with the calculated profiles. (9) In principle, a direct comparison between a microphotometer tracing of an image and its calculated (or actual) intensity profile, is not a correct procedure, since for high energy electrons the emulsion density on the photographic plate is linearly related to the incident electron intensity (and not logarithmically as is the case for photons). Instead, an intensity profile should be compared with a densitometer tracing. There are, however, numerous factors that can affect the actual image profiles, diffuse scattering in particular. The effect of the diffuse scattering, which has not been incorporated in the computer simulations, is to proportionately increase the low intensity levels much more than the near background ones. As a result, the relative differences of the intensity extremes of the actual image profiles will be much less pronounced than the theoretical ones. The exponential response of the microphotometer to emulsion densities exaggerates the intensity minima, and suppresses the maxima. The result is that the microphotometer partially compensates for the effect of diffuse scattering, so that this tracing actually appears to be closer to the calculated image profiles than a densitometer tracing. The posi-

tion, however, of the relative minima and maxima should not be affected by the diffuse scattering. It is then better to think of the dislocation image as a set of fringes parallel to the dislocation core, for which the fringe spacings is more characteristic than the fringe intensities. The criterion of agreement of fringe spacing between calculated and actual images will then be the basis for determining the value of $\vec{g}\cdot\vec{b}$. The operating vectors in a set of systematic reflections are labeled g_1, g_2, etc. and their corresponding dimensionless deviation parameters are w_1, w_2 etc. The profiles for various values of $\vec{g}_1\cdot\vec{b}$, and for various values of w_1 are then calculated for the 12-beam systematic case. In the calculations $\vec{g}$ is always the first order reflection. Other parameters are foil thickness, absorption coefficients, and position of the dislocation in the foil. In the analyzed dislocation images, the foil thickness was determined by counting the number of extinction fringes when $w_{440} = 0$. The extinction distance for a 440 reflection is about 800Å. The first order extinction distances are rather large; 2600Å for a 400 reflection, and 2150Å for a 440 reflection. The scattering potentials were computer calculated from the scattering factors of the perfect spinel lattice.

Two examples of analysis are shown in Figs. 4 and 5. In Fig. 4, the direction of the Burgers vector was determined to be <110> by the usual diffraction experiments, and under these diffraction conditions, only $\bar{g}_1\cdot\bar{b} = 1$ and $\bar{g}_1\cdot\bar{b} = 2$ are possible. From the fringe spacings of the image, i.e. separation of the subsidiary minima it can be concluded immediately that the value of $\vec{g}_1\cdot\vec{b} = 2$. A comparison between a calculated and an actual dislocation image formed with $\vec{g}_1\cdot\vec{b} = 1$, is shown in Fig. 5; in this image the geometry is such that $\vec{g}_1\cdot\vec{b} = 1$ for the undissociated

dislocation.

Fig. 5. shows an unexpected double peak in the image near the core of the dislocation. The doubling of the central fringe is only observed when the image is in focus, so that electrical charges on the dislocation, or possible magnetic inhomogeneities near the core cannot be responsible. So there is no way in which the splitting of the central fringe can be accounted for by an undissociated dislocation, even if this image is from a pure edge dislocation, and the calculated profiles are for pure screws. Instead, it must be concluded that this dislocation is probably slightly dissociated, with a partial separation of about 50 to 100Å.

These results confirm that the cation stacking fault energy is high, and that the dislocations are at most separated by about 50Å. For accurate measurements of dislocation spacings of this order, an in depth study of the contrast from closely spaced dislocations is necessary.

The ferrites that were examined here had a composition that ranged from Co/Fe = 0.54 to 0.76. The present observations do not of course rule out that for spinels outside this composition interval, the dislocations are indeed more widely separated. It is believed, however, that it can be taken as a general rule that the oxygen stacking fault energies are very high in strongly ionic crystals. This generalization is supported by observations on a number of different oxides, (10-14) although recent studies in lithium ferrite have resolved stacking faults, but not on {111} as described below.

d. Lithium Ferrite (15)

Lithium ferrite undergoes an order-disorder transformation, and so the nature of the defects depends on the state of order.

(1) Disordered $LiFe_5O_8$

Flux grown crystals of $LiFe_5O_8$, quenched from a temperature above the ordering temperature, contained areas with a high density of defects (Fig. 6). A $\bar{g}\cdot\bar{R}$ analysis on these faults showed that $\vec{R} = 1/4\langle 110\rangle$. The predominant fault plane is {110} with $\vec{R}$ always perpendicular to the fault plane. However, a few isolated examples of {112}and {123} fault planes were also found.

(2) Ordered $LiFe_5O_8$

From an analysis of the ordered structure, it could be predicted that in the ordered state, anti-phase boundaries with $\vec{R} = 1/2\ \langle 110\rangle$, would be formed. Contrast analysis using the $\alpha = 2\pi\bar{g}\cdot\bar{R}$ rule discussed in Chapter 2 (Fig. 7) is in agreement with this prediction.

These anti-phase boundaries can end on a dislocation with $b = 1/2\langle 110\rangle$ as shown in Fig. 8. In 8(a), the APB is faintly visible. The plate was taken with $w_{022} = 0$. Due to the interaction between the 011 superlattice beam and the 022 beam, the APB is visible in the 022 dark field, although $\alpha = 2\pi\bar{g}\cdot\bar{R} = 2n$. The dislocation confining the APB is split into two partials with $\vec{b} = 1/4\langle 110\rangle$ with a cation stacking fault in between. Fig. 8(b) was taken with $w_{066} = 0$. The two faults are out of contrast now and the two partials are sharply resolved.

As discussed in Chapter 2 and in the Chapter by Goringe, an advantage of using high order bright field images at high voltages is the improvement in resolution of dislocation images. The images become narrower as $\vec{n}g$ is increased. This phenomenon is clearly seen in Fig. 8(b) where the image widths are $< 50\text{Å}$.

e. Ferrimagnetic Domains in Cobalt Ferrites

In the absence of strong applied fields, all large magnetic crystals contain magnetic domains. In metals, such as cobalt and iron, these domains have usually been imaged in the electron microscope with the Lorenz method. (See Chapter by Jakubovocs) This is essentially an out-of-focus technique, in which use is made of the differently directed Lorenz forces in adjacent domains on the probing electron beam (16). The specimen is usually lifted out of the objective lens, so that it interacts less with the magnetic field of this lens. This method has the unavoidable drawback that crystal defects and domain walls cannot be observed simultaneously. In the work of deJonghe (7), the ferrimagnetic cobalt ferrite foils were in the regular specimen position, and due to the high field in the objective lens, only 90° domain walls could be present. The crystals examined were the same as those used for the dislocation analysis as discussed in section (b). Fig. 9 shows an example of ferrimagnetic domains in which the contrast is due to changes in the sign of s on crossing the walls {so called δ fringes by Amelinckx (17)}. These walls are generally associated with {110} planes and are visible mainly as a result of magnetostriction, and Lorentz contributions are negligible (7). From the change in contrast with Δs, it follows that the domains are also tetragonal twins, the tetragonality being caused by magnetostriction. This tetragonality is also detected in diffraction patterns since the Kikuchi lines are doubled.

One of the problems with these materials is that the walls are very mobile making analysis extremely tedious.

5. HIGH VOLTAGE ELECTRON MICROSCOPIC STUDIES OF MINERALS

a. On the Transformation Ortho-enstatite to Clino-enstatite

The ortho-clino inversion in enstatite ($MgSiO_3$) is interesting because the transformation from the orthorhombic to the monoclinic polymorph is dramatically promoted by shearing on (100) planes parallel to [001], but is only slightly promoted by hydrostatic compression. Earlier investigators found that clino-enstatite (CE) formed furing deformation has the $|\vec{a}^*|$ and $|\vec{b}^*|$ crystallographic axes in common with the parent ortho-enstatite (OE) and has (100)as habit plane. But they could not deduce the position of the $|\vec{c}^*|$ axis uniquely. The electron microscope study was done on a sample from a Bamble-enstatite specimen shortened 3.7% at a strain rate of 10^{-4} sec^{-1} with a confining pressure of 5 kbar and a temperature of 800°C. (18). The preparation method, ion-thinning of a preselected area, enabled correlation to be made of the electron micrographs and diffraction patterns to the oriented petrographic thin section, so that the compression direction of the deformation experiment is known on the micrographs. Electron microscopy revealed submicroscopic lamellae which are alternately OE and untwinned CE in contact on (100) habit planes and with axes $\underline{a}^*$ and $\underline{b}^*$ parallel ($|b_{OE}| = |b_{CE}|, |a_{OE}| = 2\,|a_{CE}|$). Fig. 10 displays electron micrographs of undeformed enstatite [containing stacking faults parallel to (100) in some areas] and of the deformed enstatite; the orientation of the $\underline{c}$ axis of CE with respect to the compression direction is shown in the diffraction pattern. It is the orientation made likely by the optical measurements of Trommsdorff and Wenk (19) and favored in the mechanism of Coe

(20). It contradicts the transformation mechanisms suggested by Turner et al. (21), Brown et al. (22) and Starkey (23).

b. Order in Anorthite

Calcic plagioclase feldspars with a chemical composition ranging from $Ca_{0.9}Na_{0.1}Al_{1.9}Si_{2.1}O_8$ (An 90) to $CaAl_2Si_2O_8$ (An 100) are called anorthites. Two different types of APBs may occur: Type b APBs (imaged with b-reflections: h + k odd, l odd; first observed by Christie et al., (24) and type c APBs (imaged with c-reflections: h + k even, l odd). The presence and size of antiphase domains depend on the chemical composition and the cooling history of the anorthite. A comparative study of terrestrial, meteoritic, and lunar anorthites with the high voltage microscope showed that the size of domains increases with increasing An contents in the slowly cooled metamorphic and plutonic rocks (25). Type c domains were small or not resolvable in volcanic, i.e., quenched, rocks (compare electron micrographs f and g in Fig. 11; the chemical composition is the same in the volcanic and meteoritic anorthite) (25).

Type b-APBs were absent in all terrestrial anorthites studied so far which had chemical compositions ranging from An 94 to An 100. They were present, however, in the calcic plagioclase (about An 85 to An 95) from lunar basalt 14310 (Fig. 2, first line). Most of the b-APBs were 500 to 1000 Å wide, but in rare cases larger b-domains have been observed in the same specimen. No c-domains have been resolved in anorthites from lunar sample 14310.

The antiphase vector of c-APBs was analyzed as 1/2 [$\underline{a}$ + $\underline{b}$ + $\underline{c}$]. Figure 12 shows c-APBs in anorthite from Val Pasmeda, S. Tyrol (An 100). The fringes have the properties expected for the phase factor $\alpha = \pi$,

thereby providing additional proof for the antiphase vector 1/2 [$\underline{a}$ + $\underline{b}$ + $\underline{c}$]. Calculated intensity profiles applying multi-beam dynamical theory are in agreement with the observed fringe patterns. (26)

ACKNOWLEDGEMENTS

I am grateful to students and colleagues for providing many of the illustrations used in both parts of this chapter. Their names are given in the appropriate Figure Captions. I wish to thank 1) the USAEC through the Inorganic Materials Research of the Lawrence Berkeley Laboratory for continued financial support, 2) M. Robson and D. Jurica for their attention to the electron microscopes and 3) D. Kreitz for much of the photographic work.

References Chapter

Part 2

1. D. J. Barber, J. Materials Sci., 5, 3 (1970).
2. L. C. deJonghe and G. Thomas, J. Appl. Phys., 41, 4884 (1970).
3. E. C. Snelling, Proc. Brit. Ceramic Soc., 2, 151 (1964).
4. L. C. deJonghe and G. Thomas, Mat. Sci. and Engin., 8, 259 (1971).
5. J. Hornstra, J. Phys. Chem. Solids, 15, 311 (1960).
6. M. H. Lewis, Phil. Mag., 17, 481 (1968).
7. L. C. deJonghe, Ph.D. Thesis, Univ. Calif., Berkeley, LRL Report UCRL 20369 (1970).
8. E. Levine, W. L. Bell and G. Thomas, J. Appl. Phys., 37 2141 (1966).
9. L. C. deJonghe and W. L. Bell, 75th Int. Congress Electron Microscopy, Grenoble, 2, 227 (1970).
10. M. H. Lewis, Phil. Mag., 14, 1003 (1966).
11. H. Blank and S. Amelinckx, J. Appl. Phys., 34, 2200 (1963).
12. J. Washburn, C. W. Groves, A. Kelly and G. K. Williamson, Phil. Mag., 5, 991 (1960).
13. P. Delavignette and S. Amelinckx, Appl. Phys. Letters. 2, 236 (1963).
14. C. A. May and K. H. G. Ashbee, Phil. Mag., 18, 61 (1968).
15. O. van der Biest and G. Thomas, to be published.
16. P. B. Hirsch, A. Howie, R. B. Nicholson, D. W. Pashley and M. J. Whelan, Electron Microscopy of Thin Crystals, Butterworths (1965).
17. S. Amelinckx, Modern Diffraction and Imaging Techniques in Materials Science (Eds. S. Amelinckx et al.) N. Holland, 257 (1970).
18. R. Coe and W. F. Müller, Science (in Press) (1973).
19. V. Trommsdorff and R. Wenk, Contri. Mineral. and Petrol., 19, 158-168 (1968).

20. R. Coe, Contri. Mineral. and Petrol., 26, 247 (1970).

21. F. J. Turner, H. Herd and D. T. Griggs, 21st Int. Geol. Congress, Copenhagen, Part 18, 399 (1960).

22. W. L. Brown, N. Morimoto and J. V. Smith, J. Geol., 69, 609 (1961).

23. J. Starkey, Contri. Mineral. and Petrol., 19, 133 (1968).

24. J. M. Christie, J. S. Lally, A. H. Heuer, R. M. Fisher, D. T. Griggs and S. V. Radcliffe, Geochim., Cosmochim. Acta, 1, 69 (1971).

25. W. F. Müller, H. R. Wenk and G. Thomas, Contri. Mineral. and Petrol., 34, 304 (1972).

26. W. F. Müller, H. R. Wenk, W. L. Bell and G. Thomas, Contri. Mineral. and Petrol., (in press) (1973) (LBL Report 1457).

CHAPTER FIGURE CAPTIONS

Part 2

Fig. 1. Schematic diagram of ion thinning apparatus used at Berkeley (modified after Barber Ref 1).

Fig. 2. Mass spectrometer data showing impurities in the specimen chamber environment in the Berkeley 650 kV Electron Microscope. (Ref 2 courtesy J. Appl. Physics)

Fig. 3. Proposed dislocation configuration in $(\bar{1}11)$ planes of spinels.

Fig. 4. Experimental Bright Field and computed results for a dislocation with $\bar{g}\cdot\bar{b} = 2$ in cobalt ferrite. The splitting of the central image fringe (see photometer trace) must be due to narrow two-fold dissociation. {Courtesy L. deJonghe (7,9)}

Fig. 5. As Fig. 4 for $\bar{g}\cdot\bar{b} = 1$. Again notice splitting of central image fringe. {Courtesy L. deJonghe (7,9)}

Fig. 6. Cation stacking faults on {110}in disordered $LiFe_5O_8$, giving π contrast. Notice contrast effect at overlapping faults at A (disappearance of fringes) and at intersecting faults, (fringes parallel with projected line of intersection. Bright Field (Courtesy O. van der Biest)

Fig. 7. Two bright field pictures of the same area using different "Superlattice" reflections. Contrast behavior of the APB's is consistent with a 1/2 <110> displacement vector. The fringes show π contrast symmetry. (Courtesy O. van der Biest)

Fig. 8(a). Dark field image of a dislocation decomposed into two partials and a cation stacking fault, and confining an antiphase boundary. (b) Bright field image taken from the same area with $w_{066} = 0$. Stacking faults are out of contrast ($\alpha = 2\pi n$). The image width of the dislocation is sharply reduced. Contrast in the background is

due to ion damage in the electron microscope. (Courtesy O. van der Biest)

Fig. 9. Ferrimagnetic domains in cobalt ferrite. $\vec{M}$ is the saturation magnetization inside the domains. The contrast at the domain walls is typical of δ fringes: the nature of the extreme fringes is opposite for the two walls since the sign of Δs reverses on crossing the walls. (Courtesy L. deJonghe Ref 7)

Fig. 10. High voltage electron microscopy of undeformed and deformed Bamble enstatite. Left: BF electron micrograph of an undeformed specimen showing ortho-enstatite with stacking faults parallel to (100). Center: BF electron micrograph of the deformed specimen showing alternating lamellae parallel to (100) of untwinned clino-enstatite and ortho-enstatite. Right: Selected area electron diffraction pattern corresponding to the micrograph in center showing the relation of the ortho- and clino-enstatite reciprocal axes to each other and to the compression directions (heavy arrows). 650 kV (Courtesy W. F. Müller)

Fig. 11. Structural variations in anorthites. 1st line: lunar basalt 14310; 2nd line: volcanic tuff, Japan; 3rd line: meteorite Serra de Magè; 4th line: metamorphic calesilicate rock, Alps. The electron micrographs are dark field images taken at 650 kV.

Fig. 12. Type c APBs in anorthite from S. Tyrol in bright and dark field. 650 kV

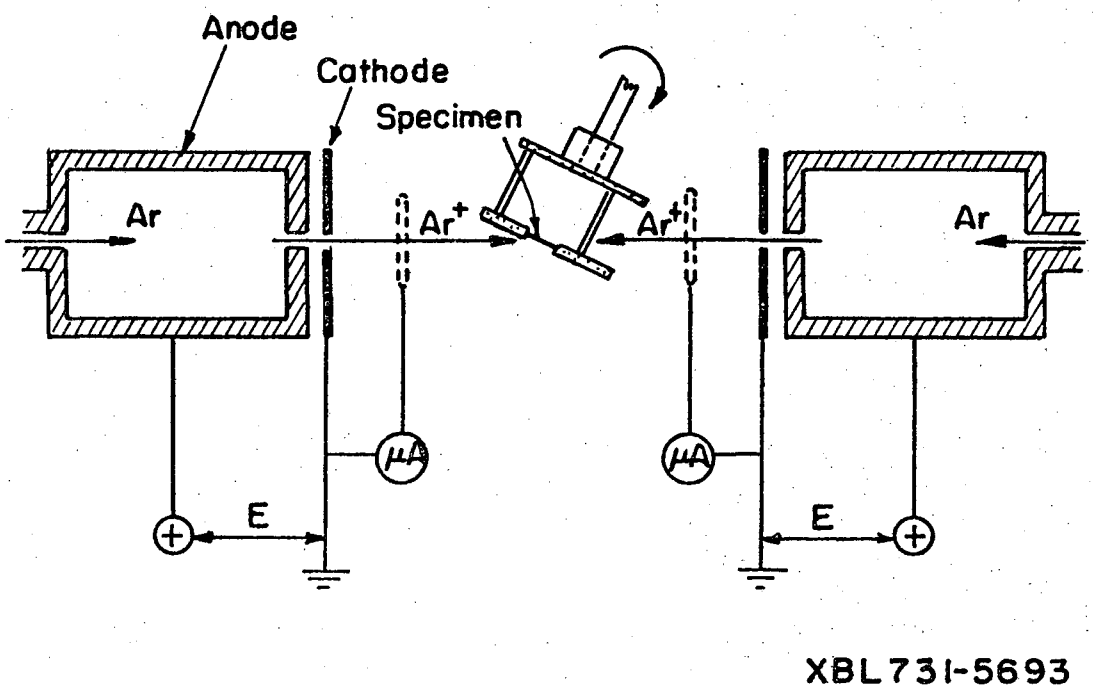

Fig. 1

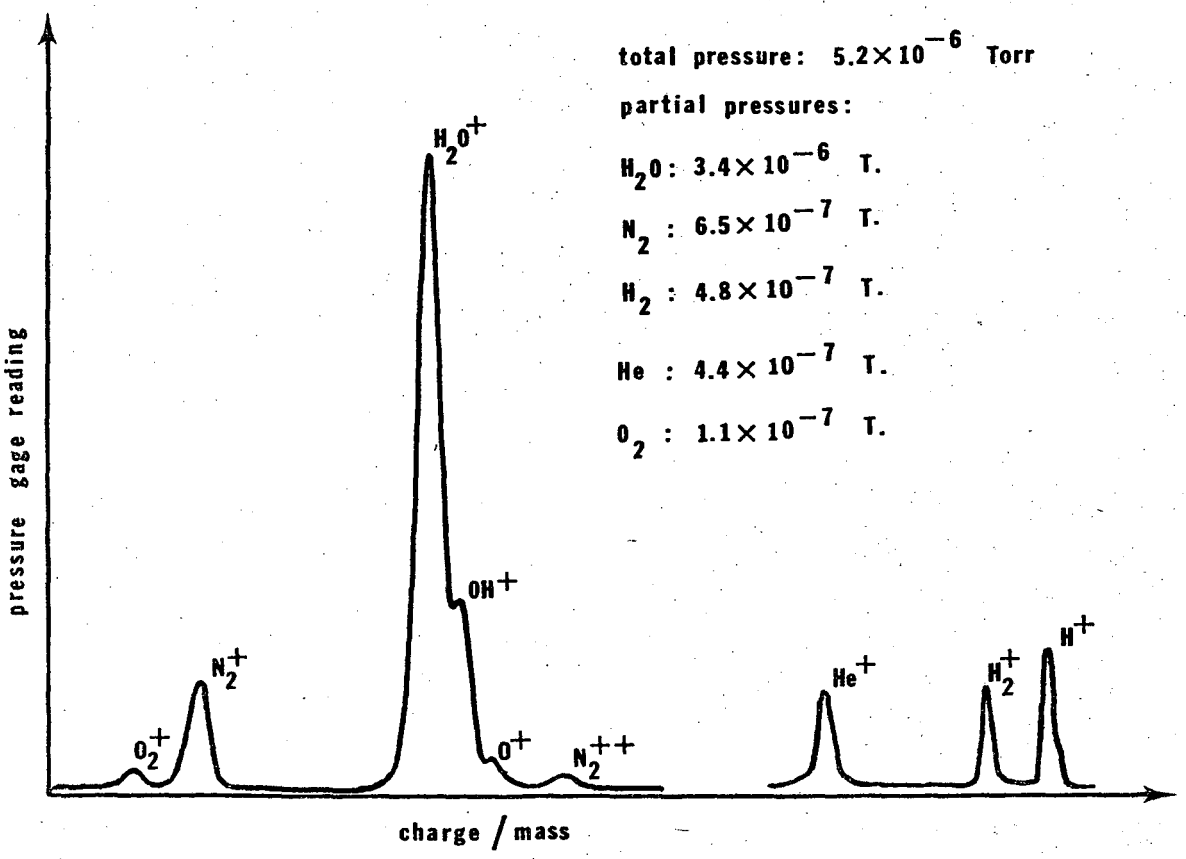

XBL 7010-6691

Fig. 2

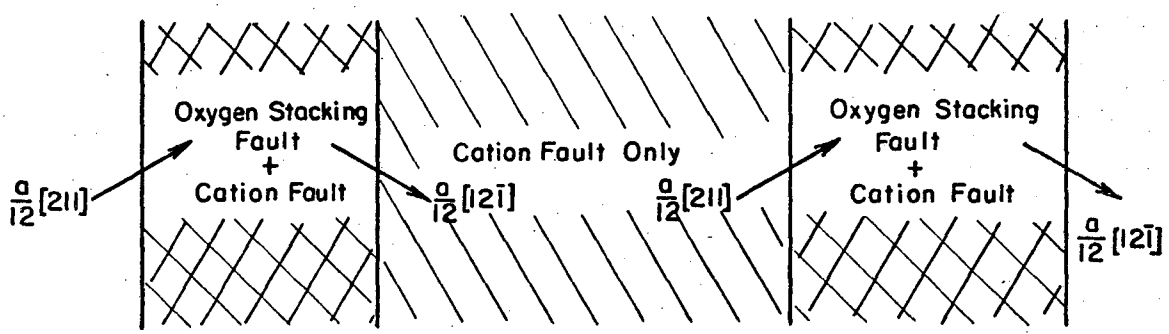

$$\frac{a}{2}[110] \rightarrow \frac{a}{4}[110] + \frac{a}{4}[110]$$

$$\frac{a}{4}[110] \rightarrow \frac{a}{12}[2\bar{1}1] + \frac{a}{12}[12\bar{1}]$$

XBL 701-205

Fig. 3

XBB 707-3328

Fig. 4

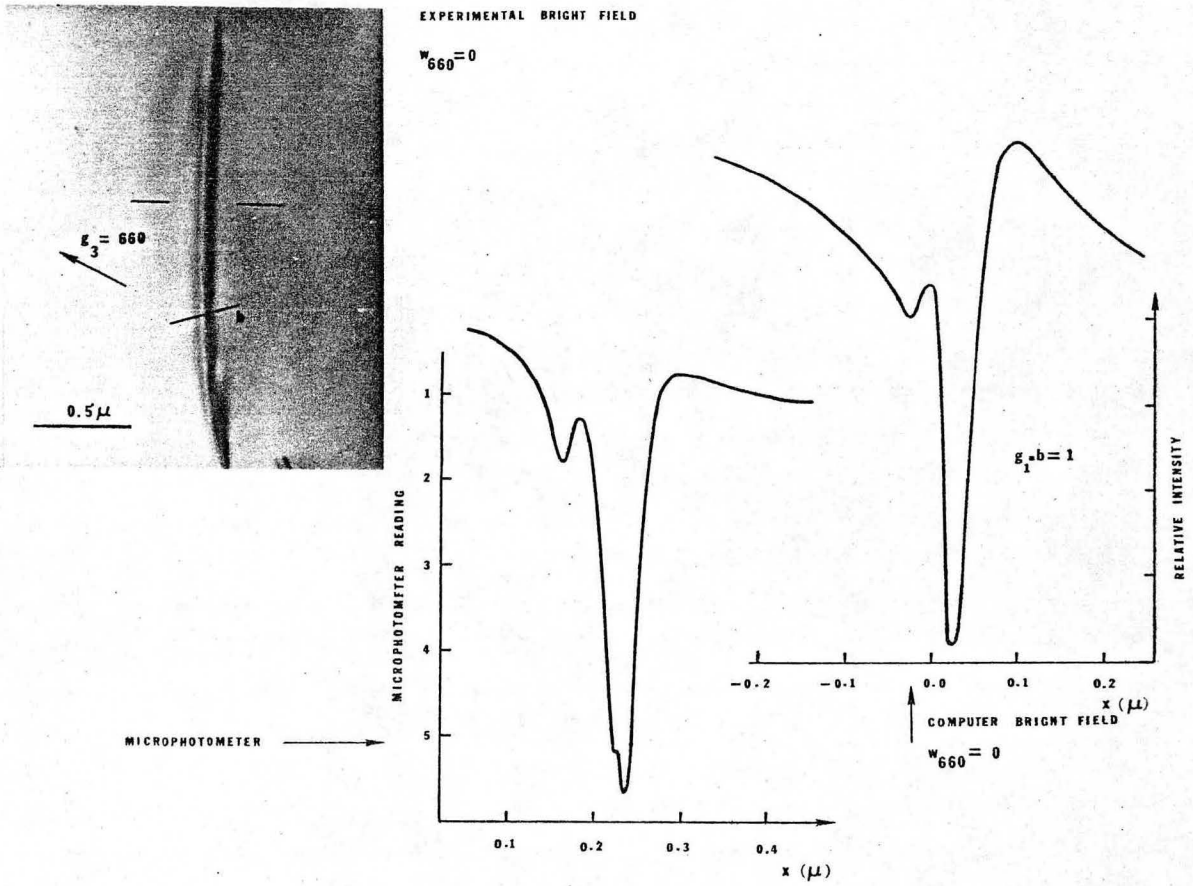

XBB 707-3329

Fig. 5

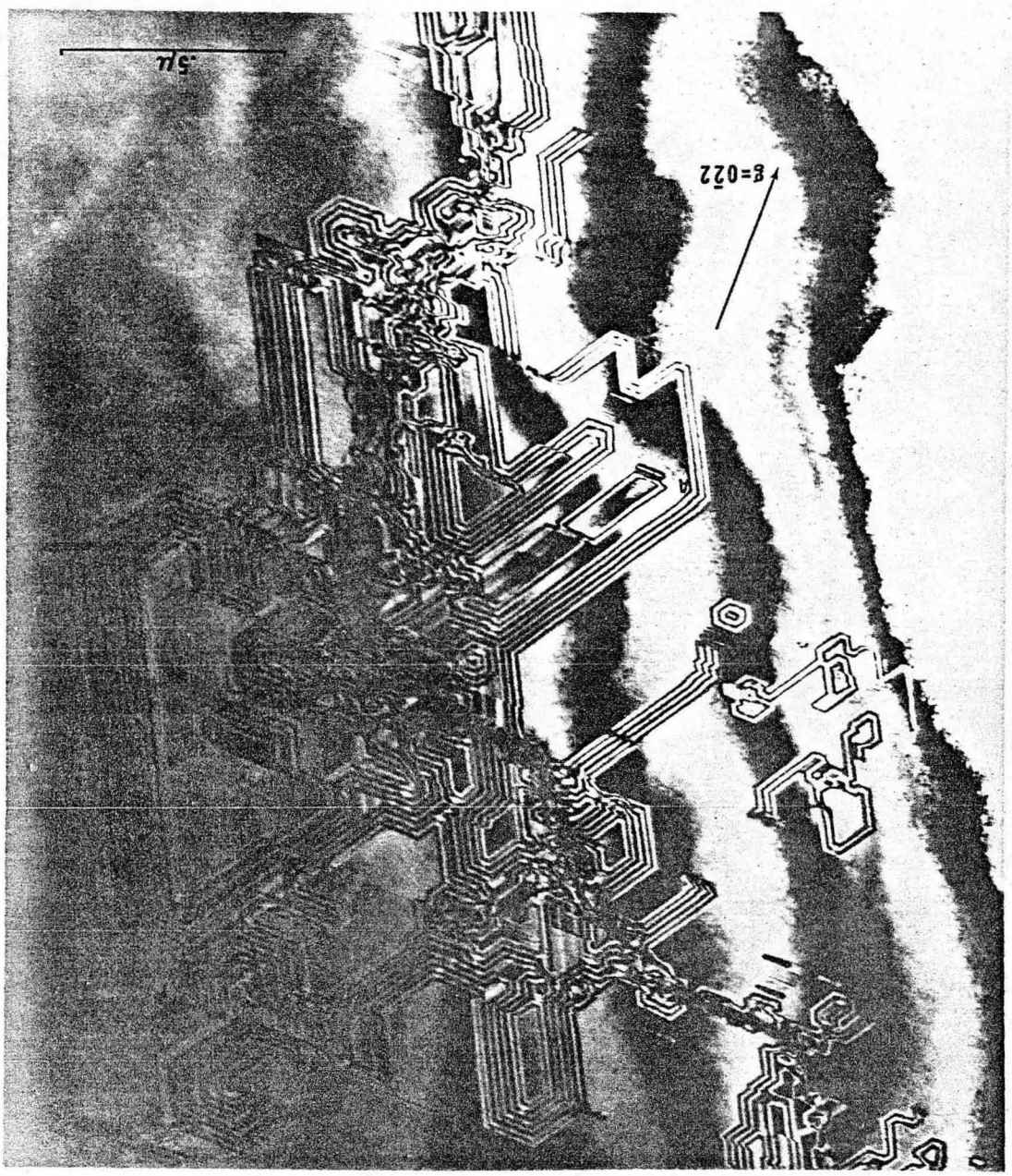

XBB 734-2443

Fig. 6

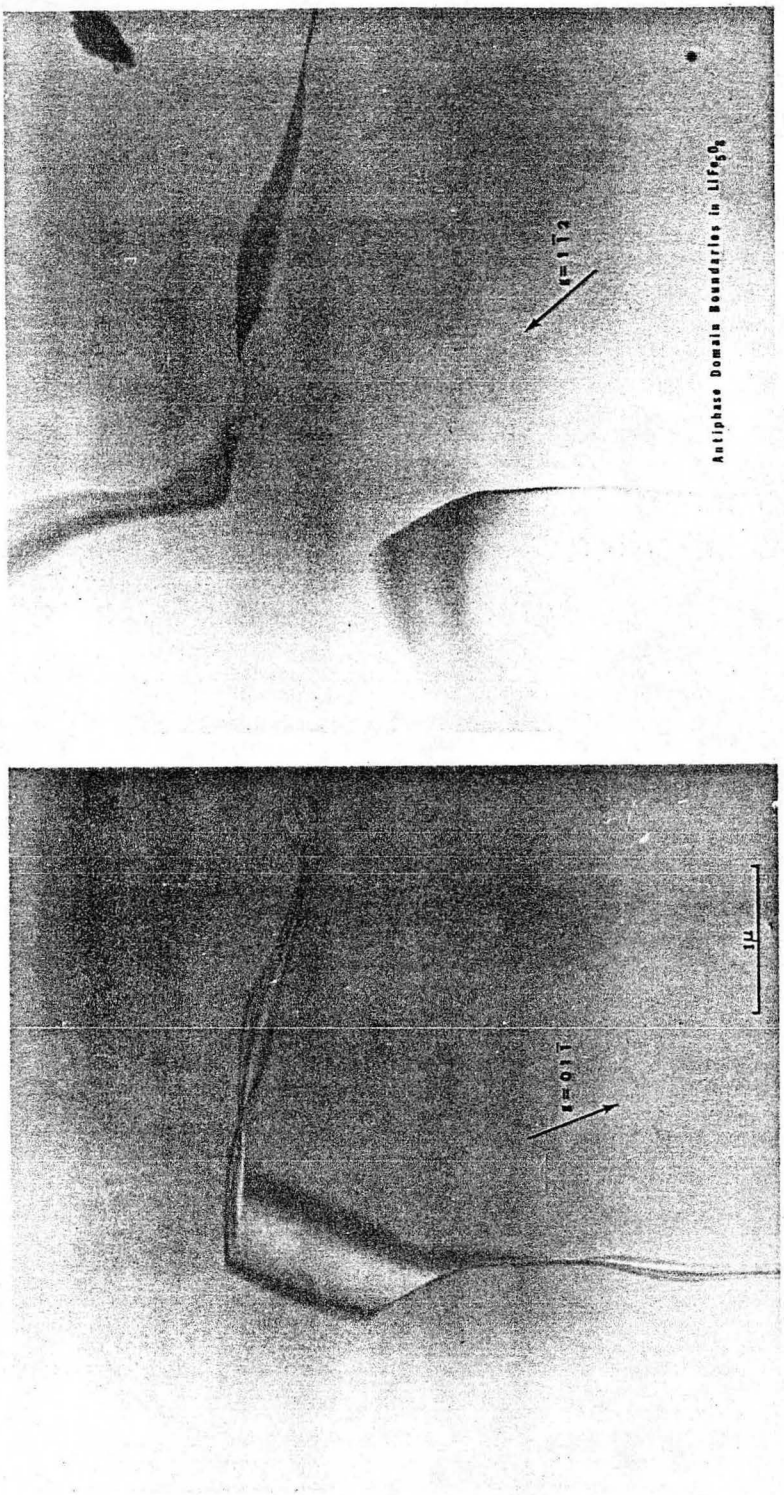

XBB 7110-4741

Fig. 7

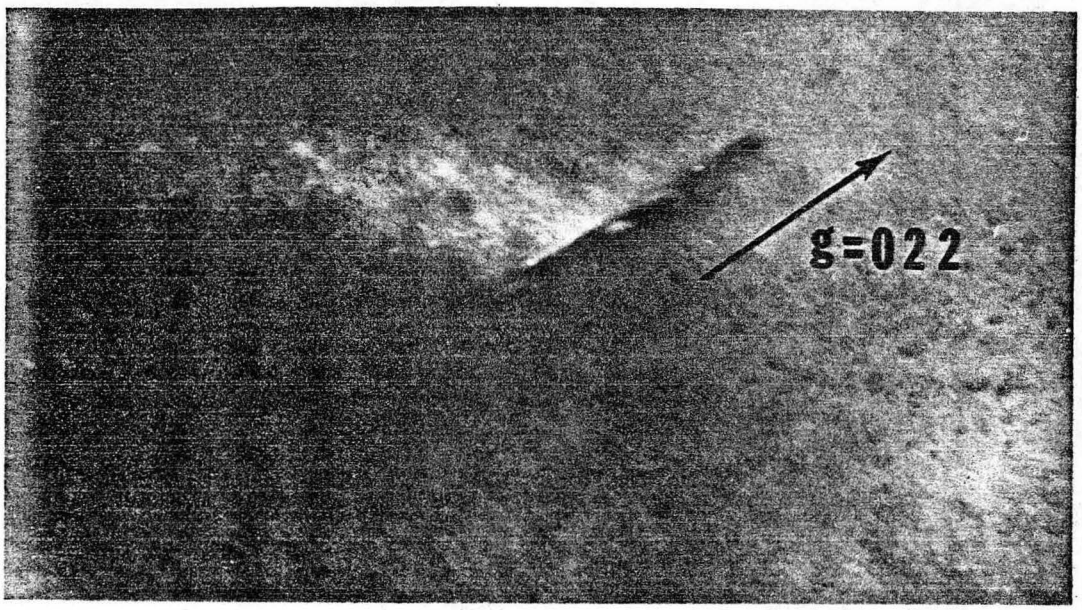

a

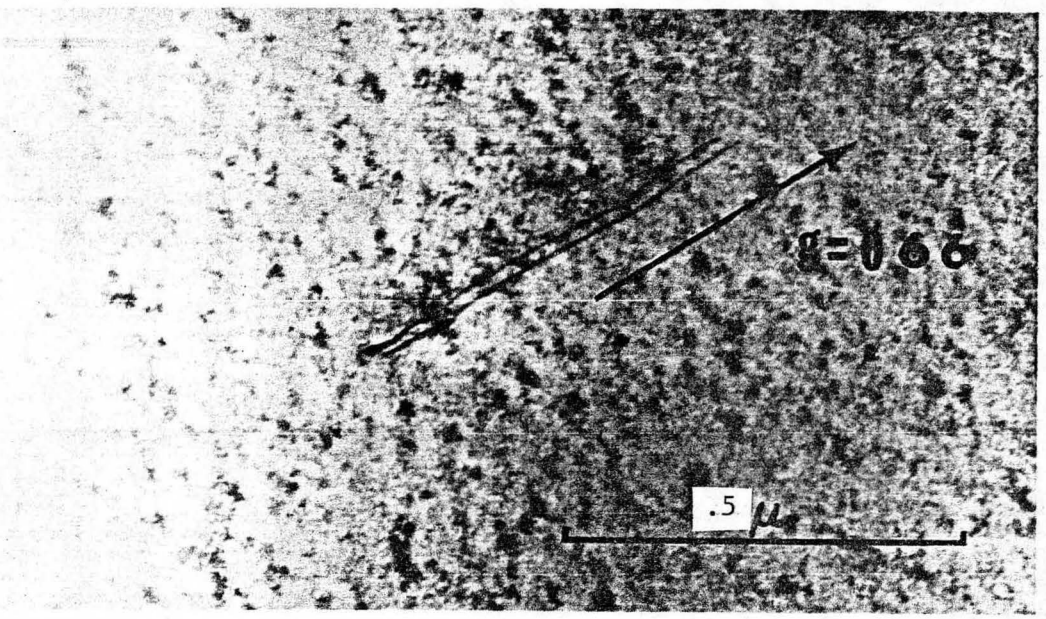

b

XBB 734-2444

Fig. 8

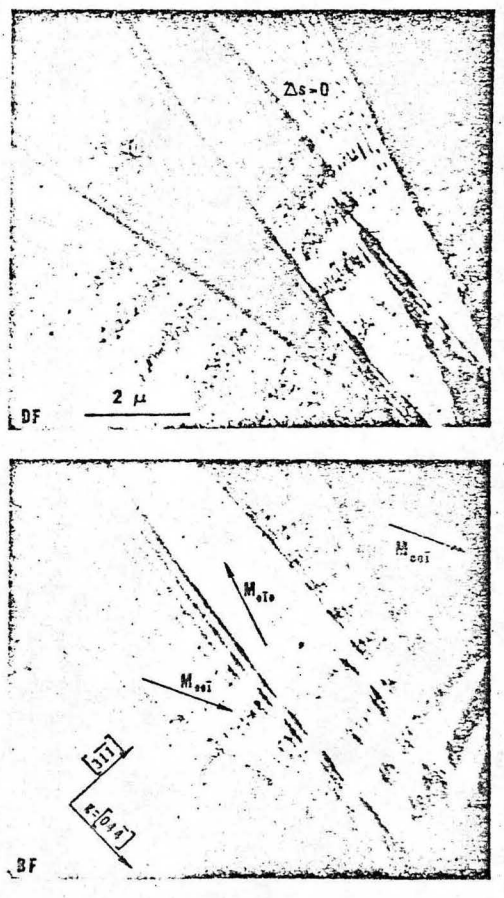

Fig. 9

XBB 706 2765

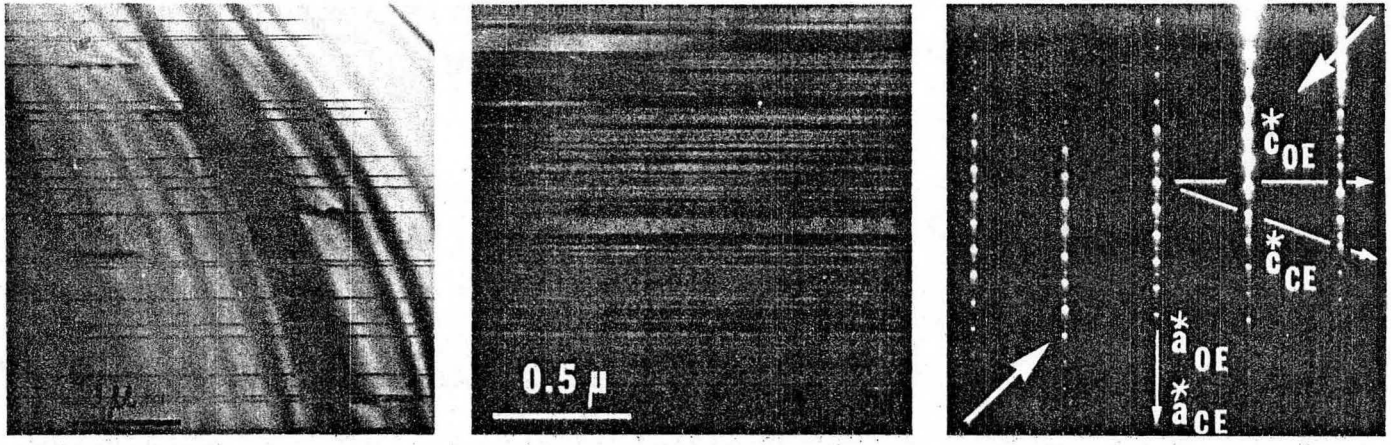

XBB 727-3691

Fig. 10

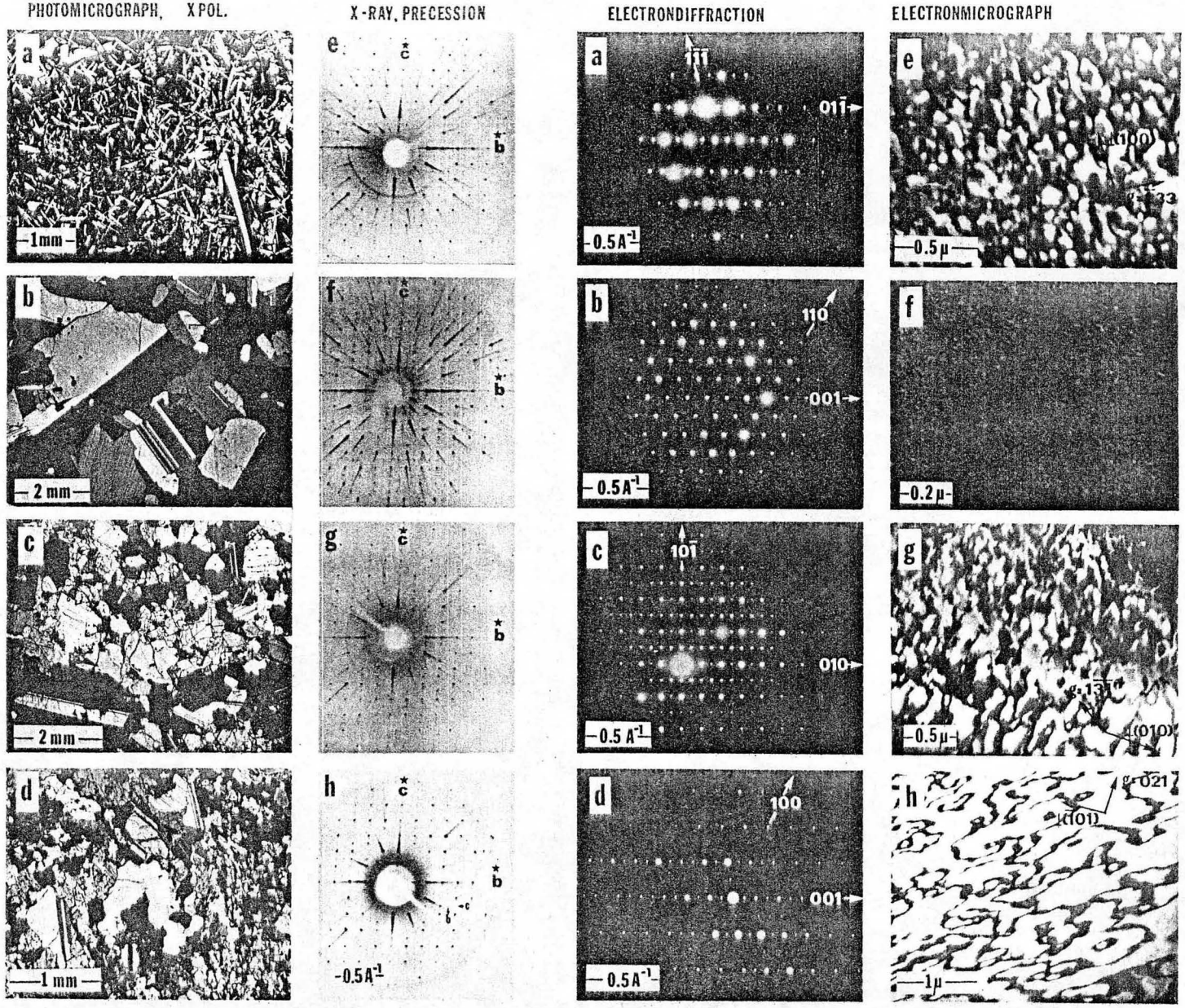

XBB 7112-6108

Fig. 11

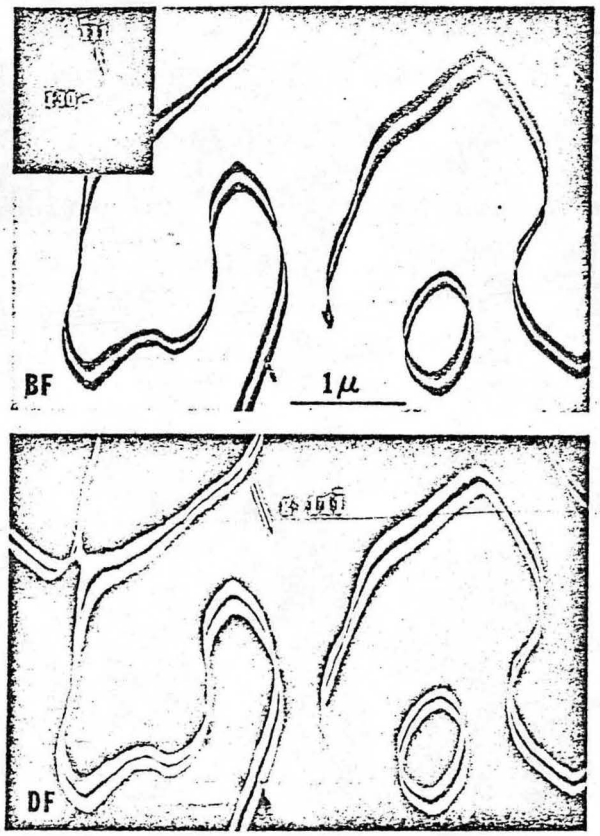

Fig. 12

TECHNICAL INFORMATION DIVISION
LAWRENCE BERKELEY LABORATORY
UNIVERSITY OF CALIFORNIA
BERKELEY, CALIFORNIA 94720